JCI The Journal of Clinical Investigation

Chromosomal 3q amplicon encodes essential regulators of secretory vesicles that drive secretory addiction in cancer

Xiaochao Tan, … , William K. Russell, Jonathan M. Kurie

J Clin Invest. 2024. https://doi.org/10.1172/JCI176355.

Research In-Press Preview Cell biology Oncology

Graphical abstract

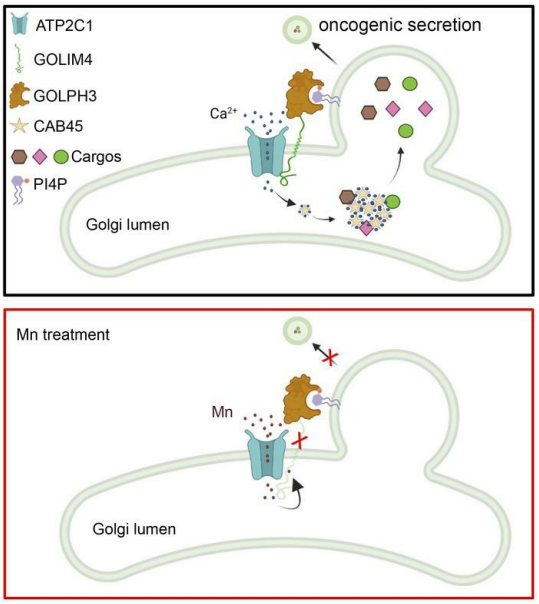

Find the latest version:

https://jci.me/176355/pdf

Chromosomal 3q amplicon encodes essential regulators of secretory vesicles that drive secretory addiction in cancer

Xiaochao Tan[1,9,10*], Shike Wang[1,9], Guan-Yu Xiao[1], Chao Wu[1], Xin Liu[1], Biyao Zhou[1], Yu Jiang[1], Dzifa Yawa Duose[2], Yuanxin Xi[3], Jing Wang[3], Kunika Gupta[4], Apar Pataer[5], Jack A Roth[5], Michael P. Kim[6], Fengju Chen[7], Chad J. Creighton[7], William K. Russell[8], Jonathan M. Kurie[1,*]

[1]Department of Thoracic/Head and Neck Medical Oncology, The University of Texas-MD Anderson Cancer Center, Houston, Texas, USA; [2]Department of Translational Molecular Pathology, The University of Texas MD Anderson Cancer Center, Houston, Texas, USA. [3]Department of Bioinformatics and Computational Biology, The University of Texas-MD Anderson Cancer Center, Houston, Texas, USA; [4]Department of Chemical Sciences, Tata Institute of Fundamental Research, 1 Homi Bhabha Road, Mumbai, India; [5]Department of Thoracic and Cardiovascular Surgery, The University of Texas MD Anderson Cancer Center, Houston, Texas, USA. [6]Department of Surgical Oncology, The University of Texas MD Anderson Cancer Center, 1515 Holcombe Boulevard, Houston, Texas, USA. [7]Department of Medicine and Dan L Duncan Cancer Center, Baylor College of Medicine, Houston, Texas, USA; [8]Department of Biochemistry and Molecular Biology, The University of Texas Medical Branch, Galveston, Texas, USA. [10]Current address: Department of Medicine, Section of Hematology and Oncology, Tulane University School of Medicine, New Orleans, LA, 70112, USA.
[9] X. Tan and S. Wang contributed equally to this work.
*To whom Correspondence should be addressed: Jonathan M. Kurie, Department of Thoracic/Head and Neck Medical Oncology, Box 432, MD Anderson Cancer Center, 1515 Holcombe Blvd, Houston, TX 77030; email: jkurie@mdanderson.org; and Xiaochao Tan, Department of Medicine, Section of Hematology and Oncology, Tulane University School of Medicine, New Orleans, LA, 70112, USA.; email: xtan4@tulane.edu.

Conflict of interest

J.M.K. has received consulting fees from Halozyme. All other authors declare that they have no competing interests.

Abstract

Cancer cells exhibit heightened secretory states that drive tumor progression. Here, we identify a chromosome 3q amplicon that serves as a platform for secretory regulation in cancer. The 3q amplicon encodes multiple Golgi-resident proteins, including the scaffold Golgi integral membrane protein 4 (GOLIM4) and the ion channel ATPase Secretory Pathway $Ca2^{+}$ Transporting 1 (ATP2C1). We show that GOLIM4 recruits ATP2C1 and Golgi phosphoprotein 3 (GOLPH3) to coordinate calcium-dependent cargo loading, Golgi membrane bending, and vesicle scission. GOLIM4 depletion disrupts the protein complex, resulting in a secretory blockade that inhibits the progression of 3q-amplified malignancies. In addition to its role as a scaffold, GOLIM4 maintains intracellular manganese (Mn) homeostasis by binding excess Mn in the Golgi lumen, which initiates the routing of Mn-bound GOLIM4 to lysosomes for degradation. We show that Mn treatment inhibits the progression of multiple types of 3q-amplified malignancies by degrading GOLIM4, resulting in a secretory blockade that interrupts pro-survival autocrine loops and attenuates pro-metastatic processes in the tumor microenvironment. Potentially underlying the selective activity of Mn against 3q-amplified malignancies, *ATP2C1* co-amplification increases Mn influx into the Golgi lumen, resulting in a more rapid degradation of GOLIM4. These findings show that functional cooperativity between co-amplified genes underlies heightened secretion and a targetable secretory addiction in 3q-amplified malignancies.

Introduction

In one working hypothesis, cancer cells are the primary architects of the tumor microenvironment (TME) (1). Despite a large body of preclinical evidence supporting their anti-tumor activities (1), strategies to neutralize matrix metalloproteinases, immune modulating cytokines, or growth factors in patients have demonstrated limited efficacy in cancer patients (2). Potentially underlying these outcomes, the cancer secretome is large and functionally redundant (3, 4). Alternative strategies designed to block the entire secretome, rather than the actions of individual secreted proteins, warrant consideration. Such approaches must be based on a thorough understanding of the way in which cancer cells acquire heightened secretory states.

Proteins destined for secretion are transported as vesicular cargos from the endoplasmic reticulum to the plasma membrane via the Golgi apparatus (5). Secretory vesicle biogenesis in the Golgi is a multi-step process involving membrane curvature, cargo loading, and vesicle scission; each step is regulated by multi-protein complexes containing RAB family members, ADP ribosylation factors, Golgi phosphoprotein 3 (GOLPH3), and other effectors (6-8). These complexes are anchored to Golgi membranes, in part, by trans-membrane Golgi scaffolds that organize client proteins dedicated to a common task (9). Golgi scaffolding proteins upregulated by p53 loss coordinate the actions of secretory drivers in p53-deficient cancer cells (10, 11). Thus, oncogenic mutations drive secretion through Golgi scaffolds that coordinate secretory vesicle biogenesis in the Golgi.

Based on evidence that co-amplified genes on chromosomal amplicons function cooperatively to coordinate common biological processes (12), we postulated here that chromosomal amplicons coordinate the multistep process of secretory vesicle biogenesis to establish heightened secretory states. We identified a region of chromosome 3q that is amplified in diverse tumor types and encodes multiple regulators of secretory vesicle biogenesis, including the Golgi scaffold Golgi integral membrane protein 4 (GOLIM4) and its client protein ATPase Secretory Pathway Ca^{2+} Transporting 1 (ATP2C1). Also known as GPP130, GOLIM4 has dual functions; it tethers endosomes to Golgi membranes, and it regulates intracellular manganese (Mn) homeostasis (13). We show that GOLIM4 and ATP2C1 cooperatively drive an addictive secretory process and thereby create a therapeutic vulnerability in 3q-amplified malignancies.

Results

GOLIM4 is a pro-tumorigenic effector of the 3q amplicon. In The Cancer Genome Atlas (TCGA), a region of chromosome 3q is amplified in, among other tumor types, squamous carcinomas of the lung (42%), esophagus (24%), and head and neck (18%). The minimally amplified region of the 3q amplicon harbors the Golgi scaffold GOLIM4 and the Golgi-resident phospholipase PLD1 (Fig. 1A). Outside of this region, the amplicon encodes ATP2C1, a Golgi-resident ion channel (14). Oncogenomic analysis demonstrated negligible convergence of the minimally amplified region with oncogenic driver mutations in lung squamous carcinoma (LUSC) (Fig. 1B) or lung adenocarcinoma (LUAD) (Fig. 1C). In TCGA lung cancer cohorts, *GOLIM4* mRNA levels are positively correlated with gene copy numbers (Fig. 1D), are higher in malignant than normal lung tissues (Fig. 1E) and are higher in metastatic deposits than primary tumors (Fig. 1F). *GOLIM4* copy numbers and mRNA levels are correlated with shorter survival durations in TCGA cohorts (Fig. 1G and H). Therefore, we developed a digital droplet PCR assay to quantify *GOLIM4* copy numbers in genomic DNA samples and showed that GOLIM4 amplification is detectable in LUSC (Fig. 1I).

To test the hypothesis that GOLIM4 is a pro-tumorigenic effector of the 3q amplicon, we first quantified GOLIM4 levels in human lung cancer cell lines classified as 3q-amplified or -diploid (15) and found that *GOLIM4* mRNA and protein levels are higher in 3q-amplified cells (Fig. 2A-C). We carried out short hairpin RNA (shRNA)- or CRISPR/CAS9-mediated *GOLIM4* depletion studies on 3q-amplified human lung cancer cells and found that GOLIM4 deficiency reduced tumor growth and metastatic activity and led to longer survival durations in mice (Fig. 2D-J and

Fig. S1A). GOLIM4-deficient tumors exhibited reduced proliferative activity and higher apoptotic fractions (Fig. S1B and C). To examine the role of GOLIM4 in an immunocompetent mouse model, we injected 129/sv mice with a syngeneic LUAD cell line (344SQ) derived from mice that express KrasG12D and p53R172H (16). These cells have increased GOLIM4 gene copy numbers (3.5 per cell) (Fig. S1D). Following CRISPR/Cas-9-mediated *GOLIM4* depletion (Fig. S1E), 344SQ cells exhibited reduced proliferative and migratory activities in culture and decreased tumor growth and metastatic activity in mice (Fig. 2K; S1F and G). In human lung cancer cell lines that are 3q-amplified or -diploid, GOLIM4 depletion reduced proliferative, migratory, and colony forming activities to a greater extent in 3q-amplified than -diploid cells (Fig. S1H-R). Similar findings were observed in breast and head and neck (HN) cancer cell lines (Fig. S2). Thus, GOLIM4 is a pro-tumorigenic effector of the 3q amplicon.

GOLIM4 activates pro-tumorigenic secretory processes. RNA sequencing studies on GOLIM4-deficient and -replete lung cancer cells showed that GOLIM4-replete cells were relatively enriched in Gene Ontology terms related to secretory processes, including 'vesicle cargo loading', 'RAB protein signal transduction', 'monocyte chemotaxis' and 'neuron axon guidance' (Fig. S3A). Therefore, we postulated that GOLIM4 activates pro-tumorigenic secretory processes and tested this hypothesis by carrying out immunohistochemical studies on GOLIM4-deficient and -replete tumors, which showed that GOLIM4 deficiency reduced endothelial cell numbers in tumor stroma (Fig. 3A). In line with these findings, conditioned medium (CM) samples from GOLIM4-replete 3q-amplified lung cancer cells chemoattracted endothelial cells and fibroblasts and rescued the viability and metastatic properties of GOLIM4-deficient 3q-amplified cells, whereas CM samples from GOLIM4-deficient cells did not have these effects (Fig. 3B-E; Fig. S3B-E).

To identify GOLIM4-dependent secreted mediators, we carried out liquid chromatography-mass spectrometry (LC-MS) analysis on CM samples from 3q-amplified human lung cancer cells that were GOLIM4-deficient or -replete and identified a total of 308 proteins, 64 of which were downregulated by GOLIM4 depletion ($P < 0.05$, fold-change >1.5 (Fig. 3F and Table S1). Western blot (WB) analysis confirmed that proteins within the downregulated group are secreted in a GOLIM4-dependent manner and showed that GOLIM4 did not regulate the expression levels of these proteins (Fig. 3G and H; Fig. S3F). Other secreted proteins identified by LC-MS analysis, such as secreted phosphoprotein 1 and stanniocalcin 2, remained unchanged following GOLIM4 depletion (Fig. S3G), suggesting that GOLIM4 controls a specific secretome.

To assess the biological role of GOLIM4-regulated secretion, we selected 10 proteins from the down-regulated group that have reported pro-tumorigenic functions (17-26) and were relatively abundant (>10 spectral counts) and found that high expression of the 10-gene signature was correlated with shorter survival durations (Fig. 3I and J). Following siRNA-mediated depletion of several members of the 10-gene signature, including amyloid precursor protein (APP), gamma glutamyl hydrolase (GGH), lysyl oxidase-like 2 (LOXL2), or pentraxin 3 (PTX3), 3q-amplified cells exhibited reduced viability, migratory activity, and colony forming activity (Fig. 3K-O). APP-deficient cells were rescued by APP-replete, but not -deficient, CM samples (Fig. S4A and B), supporting an on-target effect of the siRNA. Treatment with recombinant APP, GGH, or PTX3 proteins partially rescued the viability of GOLIM4-deficient 3q-amplified cells (Fig. S4C-E), suggesting that GOLIM4 activates autocrine signals through these proteins. In line with this conclusion, pharmacologic antagonism or siRNA-mediated depletion of γ-aminobutyric acid type B receptor 1 (GABBR1), an APP receptor (27), abrogated the ability of recombinant APP to rescue GOLIM4-deficient cells (Fig. S4F-J). Conversely, a GABBR1 agonist CGP7930 phenocopied the effects of recombinant APP on GOLIM4-deficient cells (Fig. S4G and H). Thus, GOLIM4-dependent secretion activates an APP-dependent autocrine loop that drives tumor progression.

While GOLIM4 is known to facilitate endosome-to-Golgi trafficking (28), a role in secretory vesicle biogenesis has not been reported. To address this possibility, we initially assessed GOLIM4 localization and found that it localized in the trans-Golgi network (Fig. S5A), the site of

secretory vesicle biogenesis (5). We quantified cargo loading into secretory vesicles by carrying out Golgi exit assays on cells tagged with a fluorescently tagged APP. Additionally, we quantified the total numbers of secretory vesicles in cells transfected with fluorescently tagged Rab6A, a secretory vesicle marker. These studies showed that the number of APP^+ extra-Golgi puncta per cell was reduced in GOLIM4-deficient cells (Fig. S5B), whereas the total number of $Rab6A^+$ vesicles remained unchanged (Fig. S5C), suggesting that GOLIM4 loss resulted in a cargo loading defect and an uncoupling of cargo loading from membrane budding and vesicle scission. In temperature-sensitive mutant vesicular stomatitis virus G (VSV-G) assays that quantify cargo loading and anterograde transport (27), plasma membrane bound VSV-G was reduced in GOLIM4-deficient cells (Fig. S5D), which is in line with a cargo loading defect.

To elucidate how GOLIM4 regulates cargo loading, we carried out proximity ligation assays utilizing a TurboID-GOLIM4 fusion protein as bait (Fig. 4A). LC-MS analysis of the resultant biotinylated proteins identified a total of 47 candidate interactors, including ATP2C1 (Fig. 4B and Table S2), which was confirmed to be a GOLIM4-associated protein by immunoprecipitation (IP)/WB analysis and co-immunofluorescence studies (Fig. 4C and D). ATP2C1 is a Golgi-resident Ca^{2+}/Mn^{2+} channel that interacts with cofilin1 and F-actin at the cytosolic interface to promote Ca influx into the Golgi lumen, which causes Ca-binding protein 45 kD (CAB45) to oligomerize, bind secretory cargoes, and initiate sorting of Cab45–cargo complexes into secretory vesicles (14, 29). Located on the 3q amplicon (Fig. 1A), *ATP2C1* is co-amplified with GOLIM4 (Fig. 4E), and *ATP2C1* mRNA levels are correlated with *ATP2C1* gene copy numbers and *GOLIM4* mRNA levels in TCGA lung cancer cohorts (Fig. 4F and G).

To assess the role of the ATP2C1/CAB45 axis in GOLIM4-dependent secretion, we first carried out co-IP assays and found that APP and GGH are components of a CAB45-containing protein complex (Fig. S6A). Inhibition of Ca-dependent secretion by treatment with Ca chelators decreased APP and GGH secretion (Fig. 4H; Fig. S6B). Therefore, we utilized siRNA-mediated ATP2C1 depletion as a tool to block Ca influx into the Golgi lumen, which was confirmed using a Golgi-localized Ca reporter as a readout of intra-lumenal Ca concentrations (Fig. S6C). We found that depletion of ATP2C1 or CAB45 attenuated APP and GGH secretion (Fig. 4I and J) and reduced the numbers of APP^+ extra-Golgi puncta per cell (Fig. 4K). Moreover, ATP2C1 depletion phenocopied the effect of GOLIM4 depletion in 3q-amplified lung cancer cells (Fig. 4L-P; Fig. S6D-K). An ATP2C1 mutant that lacks Ca transporter activity failed to rescue ATP2C1-deficient cells (Fig. 4Q-S). These findings support the conclusion that ATP2C1 is a GOLIM4 client that activates Ca-dependent cargo sorting to drive secretion in 3q-amplified lung cancer.

GOLIM4 exon 7 encodes a portion of the intralumenal domain and is alternatively spliced (30). To determine whether this region interacts with ATP2C1, we carried out serial deletion studies on GOLIM4 and found that ATP2C1-binding activity mapped to the intralumenal domain (Fig. S7A). A long form of *GOLIM4* that includes the alternatively spliced exon is detectable in 3q-amplified cancer cells and is reduced following depletion of RBFOX2, which drives inclusion of exon 7 (30) (Fig. 5A). In reconstitution studies carried out on GOLIM4-deficient cells, a short form of GOLIM4 that lacks the alternatively spliced exon (GOLIM4-ΔE7) did not bind to ATP2C1 (Fig. 5B and Fig. S7B) or rescue secretory, tumorigenic, or metastatic activities of GOLIM4-deficient lung cancer cells (Fig. 5C-H). In line with these findings, RBFOX2 depletion attenuated GOLIM4/ATP2C1 interactions (Fig. 5I and J; Fig. S7C) and reduced the migratory and proliferative activities of 3q-amplified lung cancer cells (Fig. 5K and L). Thus, the intraluminal domain of GOLIM4 interacts with ATP2C1 to initiate secretion.

Secretory vesicle biogenesis requires Golgi membrane bending, budding, and scission (5). GOLPH3, which bridges Golgi membranes to actomyosin fibers that initiate membrane bending (6, 7), was recently identified as a client protein of GOLIM4 (31). We found that GOLPH3 is a component of a GOLIM4-containing protein complex (Fig.6A) and that GOLIM4 is required to maintain the integrity of that complex (Fig. 6B). GOLPH3 depletion reduced secretion and the chemotactic activity of CM samples derived from 3q-amplified cells (Fig. 6C and D).

Reconstitution of GOLIM4-deficient cells with a mutant GOLIM4 lacking cytosolic domain residues (KR) required to bind GOLPH3 (31) did not rescue secretory, colony forming, or tumorigenic activities (Fig.6E-J). Thus, GOLIM4 exerts broad control of secretory vesicle biogenesis through clients that govern cargo loading and Golgi membrane bending.

Mn degrades GOLIM4 to target a secretory dependency in 3q-amplified malignancies. In addition to functioning as a scaffold, GOLIM4 maintains intracellular manganese (Mn) homeostasis by binding Mn in the Golgi lumen to generate Mn-bound GOLIM4 oligomers that are transported to lysosomes and degraded (32). To determine whether GOLIM4 functions as a Mn-binding protein in 3q-amplified cancer cells, we passed cell lysates over a Mn-binding resin and carried out LC-MS analysis on the eluted proteins, which identified a total of 10 proteins, including GOLIM4, the only Golgi-resident protein with detectable Mn-binding activity (Fig. S8A and B). Mn treatment caused GOLIM4 to translocate to lysosomes and undergo degradation, which was blocked by lysosomal but not proteasomal inhibitors (Fig. S8C and D).

To elucidate how GOLIM4 lysosomal translocation occurs, we carried out proximity ligation assays on Mn-treated cells utilizing the TurboID-GOLIM4 fusion protein as bait (Fig. S9A). By LC-MS analysis of the resultant biotinylated proteins, we identified a total of 156 candidate interactors, including, among other proteins, the BAG6/UBL4A/GET4 protein complex, which regulates membrane protein targeting and protein quality control (33), and GGA1, a member of a Golgi-localized, gamma adaptin ear-containing, ARF-binding protein family that mediates trans-membrane receptor sorting on the trans-Golgi network (34) (Fig. S9A and Table S3) . After confirming by co-IP studies that Mn causes the BAG6 complex and GGA1 to associate with GOLIM4 (Fig. S9B), we carried out siRNA-mediated depletion studies on these GOLIM4-associated proteins and found that Mn-induced GOLIM4 degradation was mitigated only by GGA1 depletion (Fig. S9C and D). In line with these findings, Mn caused GOLIM4 to translocate into GGA1-containing vesicles (Fig. S9E), and GGA1 depletion prevented GOLIM4 from leaving the Golgi and accumulating in lysosomes (Fig. S9F and G). Thus, Mn-bound GOLIM4 oligomers recruit GGA1 to initiate GOLIM4 translocation to lysosomes.

Based on these findings, we reasoned that Mn might be utilized as a targeted therapy for 3q-amplified malignancies and addressed this possibility by treating tumor-bearing mice with a Mn dose shown to be well tolerated (35). Under these conditions, Mn treatment induced no weight loss or histologic evidence of damage to major organs (Fig. S10A and B). Mn decreased intra-tumoral GOLIM4 levels irrespective of 3q amplification status but exerted greater pro-apoptotic and anti-tumor activity in 3q-amplified than -diploid models, including tumors generated by lung cancer cell lines or lung or pancreatic cancer patient-derived xenografts (Fig. 7A-E; Fig. S10C-E). In line with these findings, Mn treatment exhibited greater activity against 3q-amplified than -diploid lung, breast, and head and neck cancer cell lines in proliferation, apoptosis, and colony formation assays (Fig. 7F-J; Fig. S10F and G). Following Mn treatment, tumors generated by murine 344SQ cells in syngeneic, immunocompetent mice were smaller and less metastatic (Fig. S10H), demonstrated higher apoptotic fractions (Fig. S10I), and recruited fewer endothelial cells and fibroblasts (Fig. S10J and K). These findings are in line with evidence that GOLIM4 depletion in tumor cells inhibited endothelial cell and fibroblast chemotaxis (Fig. 3B).

To compare the efficacy of Mn to that of a proven targeted therapy, we utilized H3255 cells, which harbor a 3q amplicon and an activating EGFR mutation (L858R). Following H3255 cell injection, mice were treated daily with Mn or the EGFR antagonist Osimertinib, and tumors were measured during and after discontinuation of treatment, which showed that tumors regressed similarly following treatment with either drug (Fig. S10L). However, tumors recurred following discontinuation of Mn but not Osimertinib (Fig. S10L), suggesting that the Mn-induced anti-tumor effect was reversible. Reversible growth arrest can result from mitochondrial stress (36), which is reported to occur with Mn treatment (37). However, mitochondrial membrane integrity remained intact in Mn-treated cells (Fig. S11A-C), arguing against mitochondrial stress as a contributor to the Mn-induced growth arrest. Instead, findings from VSV-G trafficking assays (Fig. S11D), CM

transfer studies (Fig. S11E and F), and CM proteomic analysis (Fig. S11G-I) showed that Mn treatment caused a secretory blockade similar to that induced by GOLIM4 depletion.

Given that multiple Mn-binding proteins were identified in 3q-amplified lung cancer cells (S8B), we asked whether Mn exerts anti-tumor activity through GOLIM4-independent mechanisms. Arguing against this possibility, GOLIM4 depletion reduced the pro-apoptotic and anti-tumor effects of Mn treatment on 3q-amplified lung cancer cells (Fig. S11J-L). Furthermore, in GOLIM4-deficient cells reconstituted with a GOLIM4 mutant that does not bind to Mn (Fig. S11M), Mn did not degrade GOLIM4, inhibit secretion, decrease tumor cell viability or migration, or suppress tumor growth or metastasis (Fig. S11N-S). Thus, the anti-tumor effects of Mn are directly tied to GOLIM4.

While Mn induced GOLIM4 degradation irrespective of 3q amplification status (Fig. 7F), GOLIM4 degradation occurred more rapidly in 3q-amplified than -diploid lung cancer cells (Fig. 8A and B). ATP2C1 transports both Ca and Mn, which led us to speculate that *ATP2C1* amplification increases intra-Golgi Mn levels to accelerate GOLIM4 degradation. To address this possibility, we utilized a reporter assay that quantifies intra-Golgi Mn levels (38, 39) and showed that reporter activity was higher in 3q-amplified than -diploid cells and was reduced by ATP2C1 depletion in 3q-amplified cells (Fig. 8C- E; Fig. S12). Ectopic expression of wild-type ATP2C1 increased Mn reporter activity in a 3q-diploid cell line, whereas a mutant ATP2C1 that lacks transporter activity did not have this effect (Fig. 8F and G). ATP2C1 depletion abrogated Mn-induced GOLIM4 degradation in 3q-amplified cells (Fig. 8H), and ectopic co-expression of GOLIM4 and ATP2C1 sensitized a 3q-diploid lung cancer cell line (H23) to Mn treatment (Fig. 8I and J). These findings support the conclusion that *ATP2C1* co-amplification increases intra-Golgi Mn levels to hasten GOLIM4 degradation and enhance the anti-tumor effects of Mn treatment in 3q-amplified cancer cells.

Discussion

The Golgi apparatus is a complex network of membrane-bound compartments that process and sort proteins and lipids (5). Golgi scaffolds play a crucial role in maintaining the structure and function of the Golgi apparatus within cells (40, 41). For example, scaffolds organize cisternae into stacks that are essential for the proper processing and sorting of proteins and lipids (9, 42). Scaffolds also regulate the size and shape of the Golgi apparatus and are involved in vesicle tethering, fusion, and transport (40, 41, 43). More recently, scaffolds have emerged as important regulators of cancer growth and metastasis. We previously showed that the scaffolds progestin and adiponectin q receptor 11 (PAQR11) and Golgi reassembly and stacking protein 55kD (GRASP55) promote lung cancer growth and metastasis (10, 11). PAQR11 maintains a compact and polarized Golgi structure in lung cancer cells that have undergone epithelial-to-mesenchymal transition and recruits ARF1 to the Golgi membrane to facilitate vesicle formation and secretion (41). GRASP55, which plays an essential role in organizing Golgi cisternae into a stacked structure, forms a multi-protein complex that regulates the secretion of pro-tumorigenic proteins (10). In this study, we investigated the role of GOLIM4 in 3q-amplified malignancies and found that GOLIM4 recruits client proteins that coordinate secretory vesicle biogenesis and activate a heightened secretory state.

While mechanisms of secretory cargo sorting are not yet fully understood, sorting signals on cargo proteins and specific lipids within Golgi membranes play crucial roles (5). Sorting signals are recognized by specific receptors or adaptors on Golgi membranes, which recruit cargo into vesicles targeted to specific compartments (5, 44). Lipids, such as phosphoinositides and sphingolipids, also act as recognition signals for cargo sorting (45, 46). For the ATP2C1/CAB45 mediated Ca-dependent cargo sorting pathway, Ca influx into the Golgi lumen leads to the aggregation of Ca-binding protein CAB45, which binds to soluble proteins and directs their sorting into vesicles (14, 29). Our study reveals that GOLIM4 regulates secretion through this pathway.

However, elucidating the ways in which the CAB45 protein complex selects specific cargos will require further investigation.

We show that GOLIM4 activates a pro-tumorigenic secretory process and that Mn treatment depletes GOLIM4 and inhibits the loading and secretion of GOLIM4-dependent cargos. Underlying the secretory blockade induced by Mn treatment, several findings suggest that GOLIM4 depletion disrupts scaffolding functions that coordinate key drivers of secretory vesicle biogenesis. First, ATP2C1 and GOLPH3 are GOLIM4 clients that co-localize in the Golgi owing to scaffolding functions of GOLIM4. Second, ATP2C1 is co-amplified with GOLIM4, which results in high intra-Golgi Ca levels that activate a Ca-dependent cargo sorting process through ATP2C1 and its effector CAB45. Third, GOLPH3, ATP2C1, and CAB45 are required for GOLIM4-dependent cargo loading and a pro-tumorigenic secretory process activated by GOLIM4. Fourth, a GOLIM4 splice variant that cannot bind ATP2C1 does not enhance secretion or promote tumor growth, linking ATP2C1-binding activity to a pro-tumorigenic secretory process activated by GOLIM4. Fifth, a GOLIM4 mutant that cannot bind Mn does not rescue the anti-tumor effects of Mn in GOLIM4-deficient tumor cells, linking GOLIM4 to Mn-induced blockade of a pro-tumorigenic secretory process.

The underlying basis for the selective activity of Mn against 3q-amplified malignancies remains unclear, but our data point to *ATP2C1* co-amplification as a potential contributor. High ATP2C1 levels increased intra-Golgi Mn concentrations, which hastened GOLIM4 degradation and resulted in secretory blockade. Multiple GOLIM4-dependent secreted proteins maintained the viability, motility, invasion, and colony-forming activities of cancer cells, and Mn treatment inhibited the secretion of key effectors. Reconstituting those effectors through conditioned medium transfer reversed Mn-induced cell death and loss of colony forming activity, linking the 3q amplicon to an addictive secretory process.

Metal-based compounds, including platinum-based drugs and gold-based compounds, have shown promise in cancer therapy (47). These compounds can selectively interact with cancer cells or specific molecular targets to cause DNA damage, generate reactive oxygen species, and inhibit crucial enzymes (47, 48). Compared to conventional chemotherapy, metal-based targeted therapy offers potential advantages in terms of specificity and reduced toxicity (48). However, challenges remain in optimizing selectivity, delivery, understanding resistance mechanisms, and minimizing off-target effects. Mn, an essential trace element, has been found to enhance T-cell function and increase anti-tumor activity by activating the cGAS-STING pathway (49). Our study demonstrates that Mn can target cancer cells by degrading the oncoprotein GOLIM4, suggesting its potential as a targeted therapy. Nevertheless, further research is needed to evaluate treatment toxicity and identify optimal delivery routes before clinical implementation.

Several limitations of our study warrant discussion. First, we did not exhaustively investigate all 3q-encoded genes of interest, some of which may contribute to heightened secretion. Second, our short-term treatment studies did not assess the durability of therapeutic response or the development of acquired resistance to Mn. While no apparent signs of toxicity were observed, further preclinical studies are warranted to better evaluate its safety and efficacy. Third, we did not investigate the combined effects of Mn with chemotherapy or immunotherapy that could enhance the clinical applications of Mn.

In conclusion, our study identified a chromosomal amplicon that serves as a platform for secretory regulation and underlies a targetable secretory addiction. These findings lay the groundwork for therapeutic approaches aimed at disrupting the secretory process in cancer patients. The clinical relevance of 3q amplifications in cancer is underscored by their prevalence across multiple tumor types, the biological importance of a 3q-encoded functional circuitry that drives tumor progression, the availability of digital droplet PCR assays that can identify patients with 3q-amplified tumors, and the potential efficacy of Mn-based treatments.

Acknowledgments
Funding: This work was supported in part by the National Institutes of Health (R01CA236781 and R01CA255021-01) (J.M.K.), (P30CA125123) (C.K.O), U54CA224081 (J.A.R.), and (R03CA280382-01) (X.T.). The UTMB Mass Spectrometry Facility is supported in part by CPRIT grant RP190682 (to W.K.R.). J.M.K. holds the Gloria Lupton Tennison Distinguished Professorship in Lung Cancer. We thank prof. Ankona Datta for sharing the Mn sensor M1.

Author contributions: X.T. and S.W. conceived, designed, executed, and interpreted the molecular biology, cell biology, and in vivo experiments. G-Y.X. conceived, designed, executed and interpreted the VSV-G trafficking experiments. W.C. conceived, designed, and executed the *GOLIM4* and *ATP2C1* knockout cells. X.L. assisted X.T. with the *in vivo* experiments. B.Z. assisted X.T. with cell culture and western blot assays. J.Y. bred the mice for the *in vivo* studies. D.Y.D. conceived, designed, executed, and interpreted the ddPCR assay. Y.X. conceived and executed RNA sequencing data analysis. J.W. directed Y.X. on data analysis. K.G. synthesized the manganese sensor M1 and provided guidance on the manganese sensor experiment. A.P. maintained and provided the LUSC PDX. M.P.K. maintained and provided the PDAC PDX. F.C. performed the TCGA copy number analysis. C.J.C. directed and interpreted the TCGA copy number analysis. W.K.R. directed and interpreted the mass spectrometry experiments. J.M.K. conceived and supervised the project and contributed to the design and interpretation of all experiments.

Materials and Methods

Sex as a biological variant

Our study examined male mice because male animals exhibited less variability in phenotype.

Human tumor studies

Digital droplet PCR and quantitative RT-PCR assays were performed on a pre-existing tissue bank of lung squamous carcinoma and patient-derived xenograft (PDX) samples annotated based on molecular and clinical parameters.

Animal Husbandry

For subcutaneous tumor generation, nu/nu mice (5-10 mice per group) were subcutaneously injected with 1×10^6 human lung cancer cells. Orthotopic lung tumors were generated by intrathoracic injection of 1×10^6 human lung cancer cells into nu/nu mice. Frozen LUSC PDX tissues obtained from an established tissue bank at MD Anderson Cancer Center were implanted subcutaneously into NOD.Cg-Prkdc^{scid} Il2rg^{tm1Wjl}/SzJ mice (Jackson Laboratories). The resulting fresh tumors were isolated, cut into small pieces (8-10 mm^3), and transplanted into the flanks of nu/nu mice (10 mice per group). Mice were treated daily with $MnCl_2$ (50 mg/kg) or vehicle (phosphate-buffered saline) via intraperitoneal injection for a period of 2 or 3 weeks. Tumor size and mouse body weight were monitored daily. Necropsies were performed to quantify primary tumor size and assess the numbers of distant metastases.

Reagents

We purchased SYBR Green, fetal bovine serum (FBS), Dulbecco's minimal essential medium (DMEM), RPMI Media 1640, Alexa Fluor-tagged secondary antibodies, Cell-Light Golgi-RFP, and DAPI from Life Technologies; puromycin from InvivoGene; paraformaldehyde from Electron Microscopy Sciences; Transwell and Matrigel-coated Boyden chambers from BD Biosciences; G418 from Corning; CGP 54626 hydrochloride (HY-101378) and CGP7930 (HY-103502), EGTA

(HY-D0861), BAPTA (HY-100168) from MedChemExpress; shRNAs against human GOLIM4 (TRCN0000143576 and TRCN0000140441), human ATP2C1 (TRCN0000296815 and TRCN0000310147); siRNAs against human GOLIM4 (SASI_Hs02_00345751 and SASI_Hs01_00148816), human ATP2C1 (SASI_Hs01_00149544 and SASI_Hs01_00044646), human CAB45 (SASI_Hs01_00117638 and SASI_Hs01_00117639), human GOLPH3 (SASI_Hs02_00355527 and SASI_Hs01_00133692), human APP (SASI_Hs01_00185801), human FAM3C (SASI_Hs01_00053865), human FBLN1 (SASI_Hs01_00209942), human GGH (SASI_Hs01_00166929), human HTRA1 (SASI_Hs01_00055644), human LAMC2 (SASI_Hs01_00136952), human LOXL2 (SASI_Hs01_00097658), human SERPINE2 (SASI_Hs01_00144800), human TIMP1 (SASI_Hs01_00019072), human PTX3 (SASI_Hs01_00211628), human GGA1 (SASI_Hs01_00063263), human BAG6 (SASI_Hs02_00319380), human UBL4A (SASI_Hs02_00345271), human GET3 (SASI_Hs01_00233482), human GET4 (SASI_Hs01_00153734) and human TMED3 (SASI_Hs01_00024382), and siRNA Universal Negative Control #2 (SIC002) from Sigma. We purchased primary antibodies against GOLIM4 (ALX-804-603-C100) from Enzo Life Sciences; GM130 (#560066) from BD Transduction Laboratories; α-tubulin (#T9026) from Sigma; PARP-1 (#9542), cleaved-caspase 3 (#9664), and His tag (#12698) from Cell Signaling; Flag tag (F3165) and EGFP (G6539) from Sigma; hemagglutinin (HA tag) (#3724 and #2367), β-actin (#4970), GM130 (#12480), and Golgin-97 (#13192) from Cell Signaling; ATP2C1 (13310-1-AP) APP (22952-1-AP), GGH (18070-1-AP), LOXL2 (11405-1-AP), PTX3 (12306-1-AP), GGA1 (25674-1-AP), BAG6 (26417-1-AP), UBL4A (14253-1-AP), TMED3 (21902-1-AP), SPP1 (22952-1-AP), and CLU (12289-1-AP) from Proteintech; GABBR1 (ab55051) from Abcam; and VSVG (IE9F9) from Kerafast. We purchased recombinant human APP (3466-PI-010) and PTX3 (10292-TS-050) from R&D Systems; and recombinant human GGH (ab123172) from Abcam. Manganese sensor M1 was synthesized by Prof. Ankona Datta's lab (Tata Institute of Fundamental Research, Mumbai, India) and shared by them for the experiments (39).

Cell lines

Human lung cancer cell lines (A549, H1299, HCC15, H460, CALU-1, CALU-3, H358, H23, H441, H358, H596, H226, HCC95, H3255, H1819, and ABC1), human embryonic kidney 293T cells, immortalized human bronchial epithelial BEAS-2B cells, human breast cancer cell lines (MCF7, HCC70, and H1937), and human head and neck cancer cell lines (H157, FADU, and SCC25) were obtained from the American Type Culture Collection. Murine lung cancer cell lines (307P, 393P, 344P, 344SQ, and 531LN2) were generated from tumors in $Kras^{LA1/+}$;$Trp53^{R172H/+}$ mice as previously described (16). To isolate primary Thy-1 positive cancer associated fibroblasts (CAF), freshly resected primary human lung adenocarcinomas were immediately perfused with PBS containing 2% FBS. The samples were mechanically minced using a macs dissociator, followed by enzymatic digestion at 37°C for 45 minutes with collagenase type I (3mg/ml) and dispase II (4 mg/ml). The digested samples were then resuspended in PBS with 2% FBS to inactivate the enzyme. After filtration using 70 µm cell strainers and centrifugation at 400g at 4°C for 5 minutes, red blood cell (RBC) lysis was performed using 1X RBC lysis solution for 1 minute at room temperature. The samples were then washed with PBS and 2% FBS to inactivate RBC lysis, followed by another centrifugation step. The cells were resuspended in PBS with 2% FBS and counted. Cell suspension was incubated with corresponding fluorochrome-conjugated mouse anti-human primary antibodies (CD45, Thy1/CD90, CD31, EPCAM; BD Biosciences) at a 1:100 dilution for 45 minutes on ice, protected from light. After washing the cells in PBS with 2% FBS and centrifugation, compensation tubes were resuspended in 250 µL total volume, either in the presence or absence of the viability dye 7-AAD. Flow cytometry sorting was then performed to isolate CD45-negative, CD31-negative, Ep-CAM-negative, Thy-1-positive cells into 1 ml of PBS with 2% serum.

ABC1 cells, FADU cells, and CAFs were cultured in Eagle's minimal essential medium supplemented with 10% FBS. SCC25 cells were cultured in Dulbecco's MEM/Ham's F12 medium (Invitrogen), supplemented with 1 mM sodium pyruvate, 1.1 mM hydrocortisone, and 10% FBS. BEAS-2B cells, 293T cells, and MCF-7 cells were cultured in Dulbecco's MEM containing 10% FBS. HUVECs were cultured in EGM-2 Endothelial Cell Growth Medium-2 BulletKit (CC-5035, Lonza). All other human lung cancer cells and breast cancer cell lines were cultured in RPMI 1640 medium containing 10% FBS. Cells were maintained at 37°C in a humidified atmosphere with 5% CO2. Cell transfections were carried out using the jetPRIME Versatile DNA/siRNA transfection reagent (Polyplus). Stable cell transfectants were selected using puromycin (for pLKO.1 vectors) or G418 (for pcDNA3.1 and pEGFP-C3 vectors). GOLIM4 knockout (KO) H1299 cells were generated using the CRISPR-CAS9 system in the Cell-Based Assay Screening Service Core Facility at Baylor College of Medicine as previously described (10). Two guide RNAs (gRNA-1: 5'-ATCTTTGCAGAGCCAACACG-3'; gRNA-2: 5'-CAAGAACTTTCTAAGCTAAA-3') were used. GOLIM4 KO clones were confirmed by WB analysis. *ATP2C1* KO H1299 and 344SQ GOLIM4 KO cells were generated using the CRISPR-CAS9 method as previously reported (50). Briefly, for *ATP2C1* KO in H1299 cells, two single guide RNAs (sgRNA) sequence were selected from the GenScript's Broad sgRNA Database and inserted into lentiCRISPR v2 vector (gRNA-1: 5'-ATGCTTGCAACTTCACTGACTGG-3'; gRNA-2: 5'- AATATCCTCTCCATGCAATTAGG-3'); To generate *Golim4* KO 344SQ cells, two sgRNAs (gRNA-1: 5'-CACCGGTGCTTCTAACTTATAAACA-3'; gRNA-2: 5'-CACCGGCACAAGAAACACTTAACAA-3') were inserted into the lentiCRISPR v2 vector. H1299 and 344SQ cells were transfected with lentiCRISPR v2-ATP2C1/Golim4-sgRNA using jetPRIME transfection reagent. 48 h after transfection, cells were selected with puromycin for 2 days, and resulting cells were subjected to limiting dilution plating in 96-well plates for single clone isolation. The candidate clones were confirmed by WB analysis using an anti-ATP2C1 or -GOLIM4 antibody.

Vector construction

The human GOLIM4 coding sequences were isolated by performing PCR on cDNA prepared from H1299 cells and then cloned into pcDNA3.1(-) (Invitrogen). Truncations and mutations were generated by PCR method. To generate the TurboID-GOLIM4 construct, GOLIM4 coding sequences were inserted into Flag-TurboID-pcDNA3 vector using XhoI and XbaI. Primers are listed in Table S4.

The EGFP-VSV-G (ts045) expression construct (Addgene plasmid #11912) was a gift from Dr. Jennifer Lippincott-Schwartz (Janelia Research Campus, Howard Hughes Medical Institute, Ashburn, VA, USA). ATP2C1-HA-pLPCX and APT2C1-D350A-HA-pLPCX expression constructs were gifts from Dr. Julia von Blume (Yale School of Medicine, New Haven, CT, USA). EGFP-RAB6A (Addgene plasmid 49469) was a gift from Marci Scidmore (Cornell College of Veterinary Medicine, Ithaca, NY, USA). pEGFP-n1-APP (Addgene plasmid # 69924) was a gift from Zita Balklava & Thomas Wassmer (Aston University, Aston Triangle, Birmingham B4 7ET, U.K). pcDNA3.tgoGAP1 (Addgene plasmid # 78737) was a gift from Teresa Alonso (Hospital Universitario Ramón y Cajal, 28034 Madrid, Spain). GFP-GGA1 (Addgene plasmid # 178459) was a gift from Juan Bonifacino (Eunice Kennedy Shriver National Institute of Child Health and Human Development, National Institutes of Health, Bethesda, MD, USA). lentiCRISPR v2 (Addgene plasmid # 52961) was a gift from Feng Zhang (Massachusetts Institute of Technology, Cambridge, MA, USA).

Cell proliferation, colony formation, apoptosis, migration, and invasion assays

Cell proliferation assays were conducted using Cell Proliferation Reagent WST-1 (Roche), following the manufacturer's instructions. Colony formation assays at low density on plastic and in soft agarose were performed as previously described (51). Flow cytometric analysis of apoptotic cells was carried out using the Dead Cell Apoptosis Kit (Thermo Fisher Scientific,

V13242), following the manufacturer's recommended protocol. Migration and invasion assays were performed using Transwell and Matrigel-coated Boyden chambers, respectively, as previously described (11). HUVEC and CAF recruitment assays were conducted by seeding 2 × 10^4 HUVECs or 10^4 CAFs into the top chambers and H1299 cells into the bottom chambers of Transwell plates. After 12 h, the migrated HUVECs or CAFs were then stained with 0.1% crystal violet, photographed, and counted.

Western blot (WB) analysis and immunoprecipitation assays

WB analysis was performed as previously described (11). For immunoprecipitation, H1299 cells were transfected with indicated expression vectors, lysed after 48 h in 1× radioimmunoprecipitation assay buffer (RIPA buffer, Cell Signaling), and incubated with antibodies at 4 °C overnight. The immune complex was captured with protein G agarose beads (Cell signaling), washed with 1×RIPA buffer once and 1xPBS three times, and boiled in 1x sodium dodecyl sulfate loading buffer at 98 ℃ for 10 min. The resulting samples were subjected to WB analysis.

RNA sequencing

Triplicate samples of total RNA were obtained from H520 cells transfected with either siRNA against GOLIM4 or control siRNA. RNA sequencing was performed by the MD Anderson Illumina Next-Generation Sequencing Core using the NovaSeq 6000 whole transcriptome sequencing protocol. The resulting RNAseq fastq reads were mapped to the human reference genome GRCh38 (hg38) and the transcriptome gene annotation GENCODE V31 using RSEM v1.3.3. Gene expression levels were estimated based on normalized read counts in TPM (tags per million reads). The gene count data matrix was logarithmically transformed and normalized using EdgeR v3.26.8 with default settings. Differentially expressed genes between the siGOLIM4 and control groups were identified using a false discovery rate (FDR) cutoff of <= 0.05 and an absolute log2 fold change >= 1. The raw data for this study have been deposited in the NCBI's Gene Expression Omnibus database (GSE237935).

Mn pulldown assay

H1299 cells ($2X10^6$) were pre-treated with 1 mM $MnCl_2$ for 2 h and lysed in 1 ml of ice-cold RIPA buffer for 15 min on ice. For affinity purification, 80 µl of uncharged Profinity IMAC resins (#1560121, Bio-Rad) were equilibrated with sodium phosphate buffer (pH 8.0) and then incubated with the total cell lysates overnight at 4°C. After washing the resins four times with PBS, the eluted protein was subjected to LC-MS analysis or denatured in 5X SDS loading buffer at 98°C for 10 min for WB analysis.

qPCR analysis

To isolate total RNA from cells, we utilized the RNeasy Mini Kit (Qiagen). Reverse transcription was carried out using the qScript cDNA superMix (Quanta Biosciences). Genomic DNA was extracted from cells using the DNeasy Blood & Tissue Kits (Qiagen). Gene copy numbers and mRNA levels were assessed using SYBR® Green Real-Time PCR Master Mixes (Thermo Fisher Scientific) and normalized to ribosomal protein L32 (Rpl32) mRNA. The specific PCR primers used in this study are listed in Table S1.

Digital droplet PCR

GOLIM4 (5'-FAM-CACCAAGACATACATACAC-BGQ-3') and RPP30 (HEX) probes (BioRad) were diluted in BioRad ddPCR supermix and mixed with 4.4 units of HindIII restriction enzyme diluted in NEB buffer 2.1 (New England BioLabs) to make a mastermix. 10 ng of each sample was added to the mastermix in a 96 well plate. Each sample was run in duplicate. The droplets were automatically generated using the Auto-DG (BioRad) after which they were amplified in a

deep well thermocycler. The droplets were detected using QX 200 droplet reader (BioRad) and analyzed with the Quantasoft software. GOLIM4 copy number (normalized to RPP30) of each sample was determined based on the ratio of normalized PCR values.

CM sample preparation and transfer

Following a previously described protocol (52), CM samples were isolated, filtered using a 0.45-µm filter, and combined with an equal volume of complete growth medium, resulting in a final concentration of 5% FBS. This mixture was then applied to cells. In cell proliferation and colony formation assays, CM samples were replaced every two days.

LC-MS analysis

H1299 cells (2 x 10^6) were seeded in a 10-cm plate, and serum-free medium was added 24 h later. CM samples were collected after 16 h, filtered, and concentrated using Amicon Ultra-15 10K and Ultra-0.5 10K centrifugal filters. To solubilize the samples, 25 µL of 5% SDS, 50 mM TEAB (pH 7.55) was added. The solution was centrifuged at 17,000g for 10 min to remove debris. Proteins were reduced by adding 20 mM TCEP (Thermo Fisher Scientific, 77720) and incubated at 65°C for 30 min. After cooling to room temperature, 1 µL of 0.5 M iodoacetamide was added, and the solution was allowed to react in the dark for 20 min. Then, 2.75 µL of 12% phosphoric acid was added, followed by the addition of 165 µL of binding buffer (90% methanol, 100 mM TEAB, final pH 7.1). The resulting solution was passed through an S-Trap spin column (protifi.com) using a benchtop centrifuge (30-second spin at 4,000g). The spin column was washed three times with 400 µL of binding buffer. Trypsin was added to the protein mixture at a ratio of 1:25 in 50 mM TEAB (pH 8), and the solution was incubated at 37°C for 4 h. Peptides were eluted with 80 µL of 50 mM TEAB, followed by 80 µL of 0.2% formic acid, and finally 80 µL of 50% acetonitrile, 0.2% formic acid. The combined peptide solution was dried using a speed vac and then resuspended in an autosampler vial with 2% acetonitrile, 0.1% formic acid, and 97.9% water for LC-MS analysis (10). For all proteomic analysis, samples were provided as three bioreplicates.

In order to identify proteins that interact with GOLIM4, a TurboID-GOLIM4 construct was introduced into H1299 cells. After culturing in medium supplemented with or without 100 µM biotin for 1 h, cell lysates were collected, and biotinylated proteins were purified using Pierce streptavidin agarose beads from ThermoFisher Scientific. The proteins bound to the beads were then identified through LC-MS analysis, following the established protocol (52).

Secretory vesicle trafficking assays

To assess secretory vesicle biogenesis and trafficking, we carried out RAB6A-EGFP reporter assays and VSV-G trafficking assays, respectively, as previously described (52). For RAB6A-EGFP assays, live-cell imaging was conducted on RAB6A-EGFP-transfected H1299 cells, and extra-Golgi RAB6A-positive vesicles were quantified using ImageJ software. For VSV-G assays, cells were transiently transfected with EGFP-VSV-G (ts045) and subjected to a temperature shift from permissive (32 °C) to restrictive 40 °C) temperatures for 20 h. Subsequently, the cells were transferred back to the permissive temperature of 32 °C for 1 h in the presence of 100 µg/mL cycloheximide. After fixation, exofacial and total VSV-G were detected in non-permeabilized cells using an anti-VSV-G antibody and by measuring EGFP signal intensity, respectively. The trafficking of VSV-G to the plasma membrane was quantified based on a ratio of fluorescence signal from exofacial (surface) VSV-G to EGFP (total) signal intensity.

To quantify secretory cargo exit from the Golgi, H1299 cells were transiently transfected with an EGFP-tagged APP expression vector. After 24 h, the cells were incubated at a restrictive temperature of 21.5°C for 2 h in RPMI supplemented with 0.2% FBS and 100 µg/ml cycloheximide. Subsequently, the cells were transferred to a permissive temperature of 37°C and fixed at pre-determined timepoints. Cells were permeabilized and subjected to staining with

antibodies against Golgin-97 and DAPI. The APP-positive extra-Golgi puncta were counted and quantified using ImageJ.

intra-Golgi Mn and Ca assays

For intra-Golgi Mn assays, H1299 cells were transduced with CellLight Golgi-RFP (ThermoFisher) for 24 h and exposed to specified concentrations of $MnCl_2$ for 1 h before being treated with 5 μM manganese sensor M1 for 15 min. The fluorescence intensity of the M1 sensor was quantified by averaging the measured intensity within the Golgi marker region as previously reported (39). For intra-Golgi Ca assays, H1299 cells were transfected with the Calcium reporter pcDNA3.tgoGAP1 and CellLight Golgi-RFP, treated with calcium chelators EGTA (1 mM) and BAPTA (10 μM) for 4h or siRNAs against the Golgi calcium transporter ATP2C1 for 48 h. Live cell imaging was conducted using a confocal microscope. The fluorescence intensity of the Ca sensor was quantified and normalized to Golgi-RFP signals.

Microscopy and image analysis

Cells were imaged using an Eclipse Ti inverted microscope with an A1+ confocal scanner (Nikon, Japan), equipped with diode lasers of 405, 488, 561, and 640 nm wavelengths, high sensitivity Gallium arsenide phosphide and photomultiplier tube detectors, and either a 60X 1.4 NA Oil or 100X 1.45 NA Oil objective. NIS-Elements software (Nikon) version 4.40 (Build 1084) was utilized for image acquisition. For high-resolution imaging, Z-stacks were acquired sequentially with slow scan speed, using a frame size of 512x512 or 1024x1024, low pinhole, and optimized detector gain. Nyquist sampling criteria were followed, and laser power was adjusted to minimize bleaching. Post-acquisition, images were processed and deconvolved using Huygens Professional version 18.04 (Scientific Volume Imaging, The Netherlands) with the Classic Maximum Likelihood Estimation algorithm. Image analysis was performed using Fiji (ImageJ version 1.51s, NIH), Huygens Professional, or NIS-Elements. Immunofluorescence procedures were carried out following previously described (12).

Immunohistochemical analysis of tumor tissues

4 μm tissue sections from formalin-fixed and paraffin-embedded lung tissues were stained using an automated immunostainer platform, the Leica Bond Max automated stainer (Leica Biosystems Nussloch GmbH). Following the Leica Bond protocol, the tissue sections were deparaffinized and rehydrated. Antigen retrieval was performed using Bond Solution #2 (Leica Biosystems, equivalent EDTA, pH 9.0) for 30 min. Primary antibodies (CD31, dilution 1:100, Cell Signaling Technology, #77699; αSMA, dilution 1:300, Abcam, ab5694; PCNA, dilution 1:200, Cell Signaling Technology, #13110) were incubated for 15 min at room temperature. The primary antibody was detected using the Bond Polymer Refine Detection kit (Leica Biosystems) with DAB as the chromogen. Slides were counterstained with hematoxylin, dehydrated, and cover slipped. Immunostained sections were digitally scanned using the Aperio AT2 slide scanner (Leica Biosystems) under 20× objective magnification. Digital image analysis was performed using pathologist-trained specific algorithms for quantification.

Statistical analysis

Unless stated otherwise, the results shown are representative of replicated experiments and are the means ± standard deviations from triplicate samples or randomly chosen cells within a field. Statistical evaluations were carried out with Prism 6 (GraphPad Software, Inc.). Unpaired 2-tailed Stuof secretory vesicle biogedent t-tests were used to compare the mean values of 2 groups. ANOVA with Dunnett's test was used for comparing multiple treatments to a control. P values < 0.05 were considered statistically significant. Kaplan-Meier survival data were generated using GEPIA2 (53) or cBioportal (54-56). Plots were generated for the respective groups using Graphpad Prism version 9.

Study approval

Human tumor specimens were obtained through an IRB-approved protocol and informed consent, and the analysis of the human tissue specimens was approved by an Institutional Review Board at MD Anderson Cancer Center. All mouse studies were conducted in accordance with the guidelines and regulations approved by the Institutional Animal Care and Use Committee at The University of Texas MD Anderson Cancer Center. Mice received standard care and were euthanized according to the established protocols of the Institutional Animal Care and Use Committee.

Data availability

The RNA-seq data are available in the NCBI's Gene Expression Omnibus database (GSE237935). All other data associated with this study are present in the manuscript or in the Supplementary Materials and are available in the “supporting data values” xls file.

References

1. Li J, and Stanger BZ. The tumor as organizer model. *Science.* 2019;363(6431):1038-9.
2. Paltridge JL, Belle L, and Khew-Goodall Y. The secretome in cancer progression. *Biochim Biophys Acta.* 2013;1834(11):2233-41.
3. Quail DF, and Joyce JA. Microenvironmental regulation of tumor progression and metastasis. *Nat Med.* 2013;19(11):1423-37.
4. Coussens LM, Fingleton B, and Matrisian LM. Matrix metalloproteinase inhibitors and cancer: trials and tribulations. *Science.* 2002;295(5564):2387-92.
5. Kienzle C, and von Blume J. Secretory cargo sorting at the trans-Golgi network. *Trends Cell Biol.* 2014;24(10):584-93.
6. Dippold HC, Ng MM, Farber-Katz SE, Lee SK, Kerr ML, Peterman MC, et al. GOLPH3 bridges phosphatidylinositol-4- phosphate and actomyosin to stretch and shape the Golgi to promote budding. *Cell.* 2009;139(2):337-51.
7. Rahajeng J, Kuna RS, Makowski SL, Tran TTT, Buschman MD, Li S, et al. Efficient Golgi Forward Trafficking Requires GOLPH3-Driven, PI4P-Dependent Membrane Curvature. *Dev Cell.* 2019;50(5):573-85 e5.
8. Valente C, Polishchuk R, and De Matteis MA. Rab6 and myosin II at the cutting edge of membrane fission. *Nat Cell Biol.* 2010;12(7):635-8.
9. Kulkarni-Gosavi P, Makhoul C, and Gleeson PA. Form and function of the Golgi apparatus: scaffolds, cytoskeleton and signalling. *FEBS Lett.* 2019;593(17):2289-305.
10. Tan X, Shi L, Banerjee P, Liu X, Guo HF, Yu J, et al. A protumorigenic secretory pathway activated by p53 deficiency in lung adenocarcinoma. *J Clin Invest.* 2021;131(1).
11. Tan X, Banerjee P, Shi L, Xiao GY, Rodriguez BL, Grzeskowiak CL, et al. p53 loss activates prometastatic secretory vesicle biogenesis in the Golgi. *Sci Adv.* 2021;7(25).
12. Tan X, Banerjee P, Pham EA, Rutaganira FUN, Basu K, Bota-Rabassedas N, et al. PI4KIIIbeta is a therapeutic target in chromosome 1q-amplified lung adenocarcinoma. *Sci Transl Med.* 2020;12(527).
13. Venkat S, and Linstedt AD. Manganese-induced trafficking and turnover of GPP130 is mediated by sortilin. *Mol Biol Cell.* 2017;28(19):2569-78.
14. von Blume J, Alleaume AM, Cantero-Recasens G, Curwin A, Carreras-Sureda A, Zimmermann T, et al. ADF/cofilin regulates secretory cargo sorting at the TGN via the Ca2+ ATPase SPCA1. *Dev Cell.* 2011;20(5):652-62.

15. Tsherniak A, Vazquez F, Montgomery PG, Weir BA, Kryukov G, Cowley GS, et al. Defining a Cancer Dependency Map. *Cell.* 2017;170(3):564-76 e16.
16. Gibbons DL, Lin W, Creighton CJ, Rizvi ZH, Gregory PA, Goodall GJ, et al. Contextual extracellular cues promote tumor cell EMT and metastasis by regulating miR-200 family expression. *Genes Dev.* 2009;23(18):2140-51.
17. Giacomini A, Ghedini GC, Presta M, and Ronca R. Long pentraxin 3: A novel multifaceted player in cancer. *Biochim Biophys Acta Rev Cancer.* 2018;1869(1):53-63.
18. Wen B, Xu LY, and Li EM. LOXL2 in cancer: regulation, downstream effectors and novel roles. *Biochim Biophys Acta Rev Cancer.* 2020;1874(2):188435.
19. Wu L, Li X, Li Z, Cheng Y, Wu F, Lv C, et al. HtrA serine proteases in cancers: A target of interest for cancer therapy. *Biomed Pharmacother.* 2021;139:111603.
20. Lim S, Yoo BK, Kim HS, Gilmore HL, Lee Y, Lee HP, et al. Amyloid-beta precursor protein promotes cell proliferation and motility of advanced breast cancer. *BMC Cancer.* 2014;14:928.
21. Shubbar E, Helou K, Kovacs A, Nemes S, Hajizadeh S, Enerback C, et al. High levels of gamma-glutamyl hydrolase (GGH) are associated with poor prognosis and unfavorable clinical outcomes in invasive breast cancer. *BMC Cancer.* 2013;13:47.
22. Zhang J, Wu Q, Zhu L, Xie S, Tu L, Yang Y, et al. SERPINE2/PN-1 regulates the DNA damage response and radioresistance by activating ATM in lung cancer. *Cancer Lett.* 2022;524:268-83.
23. Garg M, Braunstein G, and Koeffler HP. LAMC2 as a therapeutic target for cancers. *Expert Opin Ther Targets.* 2014;18(9):979-82.
24. Gong J, Jie Y, Xiao C, Zhou W, Li X, Chen Y, et al. Increased Expression of Fibulin-1 Is Associated With Hepatocellular Carcinoma Progression by Regulating the Notch Signaling Pathway. *Front Cell Dev Biol.* 2020;8:478.
25. Duch P, Diaz-Valdivia N, Ikemori R, Gabasa M, Radisky ES, Arshakyan M, et al. Aberrant TIMP-1 overexpression in tumor-associated fibroblasts drives tumor progression through CD63 in lung adenocarcinoma. *Matrix Biol.* 2022;111:207-25.
26. Thuya WL, Kong LR, Syn NL, Ding LW, Cheow ESH, Wong RTX, et al. FAM3C in circulating tumor-derived extracellular vesicles promotes non-small cell lung cancer growth in secondary sites. *Theranostics.* 2023;13(2):621-38.
27. Rice HC, de Malmazet D, Schreurs A, Frere S, Van Molle I, Volkov AN, et al. Secreted amyloid-beta precursor protein functions as a GABA(B)R1a ligand to modulate synaptic transmission. *Science.* 2019;363(6423).
28. Natarajan R, and Linstedt AD. A cycling cis-Golgi protein mediates endosome-to-Golgi traffic. *Mol Biol Cell.* 2004;15(11):4798-806.
29. Crevenna AH, Blank B, Maiser A, Emin D, Prescher J, Beck G, et al. Secretory cargo sorting by Ca2+-dependent Cab45 oligomerization at the trans-Golgi network. *J Cell Biol.* 2016;213(3):305-14.
30. Luo CL, Xu XC, Liu CJ, He S, Chen JR, Feng YC, et al. RBFOX2/GOLIM4 Splicing Axis Activates Vesicular Transport Pathway to Promote Nasopharyngeal Carcinogenesis. *Adv Sci (Weinh).* 2021;8(16):e2004852.
31. Welch LG, Peak-Chew SY, Begum F, Stevens TJ, and Munro S. GOLPH3 and GOLPH3L are broad-spectrum COPI adaptors for sorting into intra-Golgi transport vesicles. *J Cell Biol.* 2021;220(10).
32. Tewari R, Jarvela T, and Linstedt AD. Manganese induces oligomerization to promote down-regulation of the intracellular trafficking receptor used by Shiga toxin. *Mol Biol Cell.* 2014;25(19):3049-58.
33. Hessa T, Sharma A, Mariappan M, Eshleman HD, Gutierrez E, and Hegde RS. Protein targeting and degradation are coupled for elimination of mislocalized proteins. *Nature.* 2011;475(7356):394-7.

34. Doray B, Ghosh P, Griffith J, Geuze HJ, and Kornfeld S. Cooperation of GGAs and AP-1 in packaging MPRs at the trans-Golgi network. *Science.* 2002;297(5587):1700-3.
35. Mukhopadhyay S, and Linstedt AD. Manganese blocks intracellular trafficking of Shiga toxin and protects against Shiga toxicosis. *Science.* 2012;335(6066):332-5.
36. Wang SF, Tseng LM, and Lee HC. Role of mitochondrial alterations in human cancer progression and cancer immunity. *J Biomed Sci.* 2023;30(1):61.
37. Harischandra DS, Ghaisas S, Zenitsky G, Jin H, Kanthasamy A, Anantharam V, et al. Manganese-Induced Neurotoxicity: New Insights Into the Triad of Protein Misfolding, Mitochondrial Impairment, and Neuroinflammation. *Front Neurosci.* 2019;13:654.
38. Das S, Carmona A, Khatua K, Porcaro F, Somogyi A, Ortega R, et al. Manganese Mapping Using a Fluorescent Mn(2+) Sensor and Nanosynchrotron X-ray Fluorescence Reveals the Role of the Golgi Apparatus as a Manganese Storage Site. *Inorg Chem.* 2019;58(20):13724-32.
39. Bakthavatsalam S, Sarkar A, Rakshit A, Jain S, Kumar A, and Datta A. Tuning macrocycles to design 'turn-on' fluorescence probes for manganese(II) sensing in live cells. *Chem Commun (Camb).* 2015;51(13):2605-8.
40. Xiang Y, and Wang Y. GRASP55 and GRASP65 play complementary and essential roles in Golgi cisternal stacking. *J Cell Biol.* 2010;188(2):237-51.
41. Tan X, Banerjee P, Guo HF, Ireland S, Pankova D, Ahn YH, et al. Epithelial-to-mesenchymal transition drives a pro-metastatic Golgi compaction process through scaffolding protein PAQR11. *J Clin Invest.* 2017;127(1):117-31.
42. Xiang Y, Zhang X, Nix DB, Katoh T, Aoki K, Tiemeyer M, et al. Regulation of protein glycosylation and sorting by the Golgi matrix proteins GRASP55/65. *Nat Commun.* 2013;4:1659.
43. D'Angelo G, Prencipe L, Iodice L, Beznoussenko G, Savarese M, Marra P, et al. GRASP65 and GRASP55 sequentially promote the transport of C-terminal valine-bearing cargos to and through the Golgi complex. *J Biol Chem.* 2009;284(50):34849-60.
44. Ramazanov BR, Tran ML, and von Blume J. Sending out molecules from the TGN. *Curr Opin Cell Biol.* 2021;71:55-62.
45. Deng Y, Pakdel M, Blank B, Sundberg EL, Burd CG, and von Blume J. Activity of the SPCA1 Calcium Pump Couples Sphingomyelin Synthesis to Sorting of Secretory Proteins in the Trans-Golgi Network. *Dev Cell.* 2018;47(4):464-78 e8.
46. von Blume J, and Hausser A. Lipid-dependent coupling of secretory cargo sorting and trafficking at the trans-Golgi network. *FEBS Lett.* 2019;593(17):2412-27.
47. Ndagi U, Mhlongo N, and Soliman ME. Metal complexes in cancer therapy - an update from drug design perspective. *Drug Des Devel Ther.* 2017;11:599-616.
48. Frezza M, Hindo S, Chen D, Davenport A, Schmitt S, Tomco D, et al. Novel metals and metal complexes as platforms for cancer therapy. *Curr Pharm Des.* 2010;16(16):1813-25.
49. Lv M, Chen M, Zhang R, Zhang W, Wang C, Zhang Y, et al. Manganese is critical for antitumor immune responses via cGAS-STING and improves the efficacy of clinical immunotherapy. *Cell Res.* 2020;30(11):966-79.
50. Sanjana NE, Shalem O, and Zhang F. Improved vectors and genome-wide libraries for CRISPR screening. *Nat Methods.* 2014;11(8):783-4.
51. Tan X, Banerjee P, Liu X, Yu J, Gibbons DL, Wu P, et al. The epithelial-to-mesenchymal transition activator ZEB1 initiates a prometastatic competing endogenous RNA network. *J Clin Invest.* 2018;128(7):3198.
52. Tan X, Xiao GY, Wang S, Shi L, Zhao Y, Liu X, et al. EMT-activated secretory and endocytic vesicular trafficking programs underlie a vulnerability to PI4K2A antagonism in lung cancer. *J Clin Invest.* 2023;133(7).

53. Tang Z, Kang B, Li C, Chen T, and Zhang Z. GEPIA2: an enhanced web server for large-scale expression profiling and interactive analysis. *Nucleic Acids Res.* 2019;47(W1):W556-W60.
54. Cerami E, Gao J, Dogrusoz U, Gross BE, Sumer SO, Aksoy BA, et al. The cBio cancer genomics portal: an open platform for exploring multidimensional cancer genomics data. *Cancer Discov.* 2012;2(5):401-4.
55. de Bruijn I, Kundra R, Mastrogiacomo B, Tran TN, Sikina L, Mazor T, et al. Analysis and Visualization of Longitudinal Genomic and Clinical Data from the AACR Project GENIE Biopharma Collaborative in cBioPortal. *Cancer Res.* 2023;83(23):3861-7.
56. Gao J, Aksoy BA, Dogrusoz U, Dresdner G, Gross B, Sumer SO, et al. Integrative analysis of complex cancer genomics and clinical profiles using the cBioPortal. *Sci Signal.* 2013;6(269):pl1.

Figures and legends

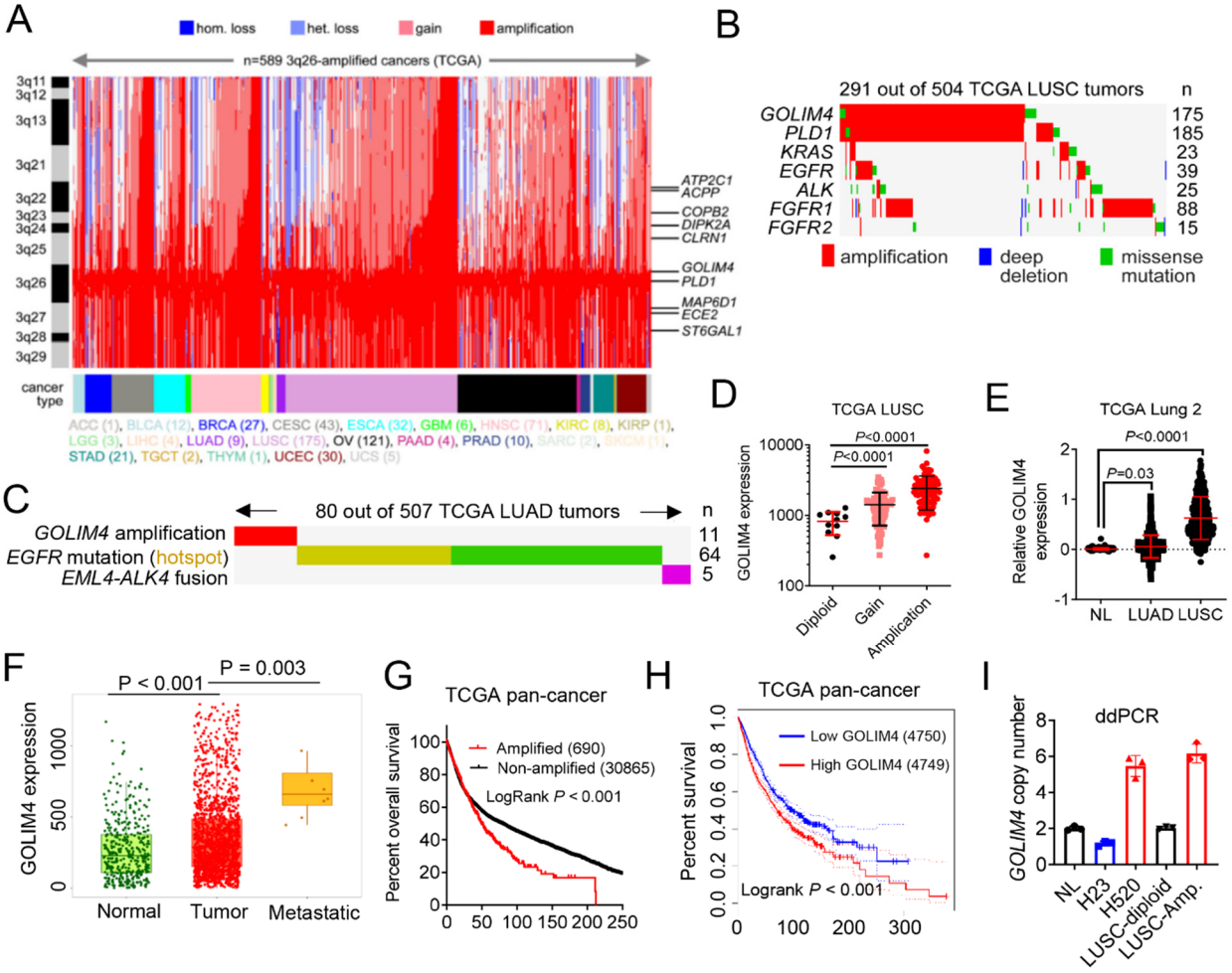

Figure 1. Oncogenomic analysis of the 3q amplicon in human cancers. (A) Heat map illustration of 3q-encoded gene copy numbers (Y axis) in TCGA pan-cancer cohort (n=589, X axis). Genomic regions are color-coded based on copy number change and tumor type. (B and C) Somatic mutations (rows) in TCGA lung squamous carcinoma (LUSC) (B) and lung adenocarcinoma (LUAD) (C) cohorts (columns). (D) Correlation of *GOLIM4* mRNA levels and gene copy numbers in TCGA LUSC samples (dots). Diploid (n = 50), gain (n = 238), and amplification (n = 208). (E) *GOLIM4* mRNA levels in normal lung tissues (NL) (n = 397), LUAD (n = 492), and LUSC (n = 488). (F) *GOLIM4* mRNA levels in NL tissues (n=3691), primary lung tumors (n=1865), and distant metastases (n=8) (https://tnmplot.com/). Box plots represent 33% (lower box) and 66% (upper box). P values, Dunn's test. (G and H) Kaplan-Meier survival analysis of TCGA pan-cancer cohort based on GOLIM4 copy numbers (G) and mRNA levels (H). (I) Digital droplet PCR assay of GOLIM4 copy numbers in NL tissues and 3q-amplified (Amp) and -diploid LUSC tissues. Controls

include 3q-amplified (H520) and -diploid (H23) cell lines. Data indicate the mean ± SD from a single experiment incorporating biological replicate samples (n = 3, unless otherwise indicated) and are representative of at least 2 independent experiments. P values were determined using One-way ANOVA test (for D-F) or logrank test (for G and H).

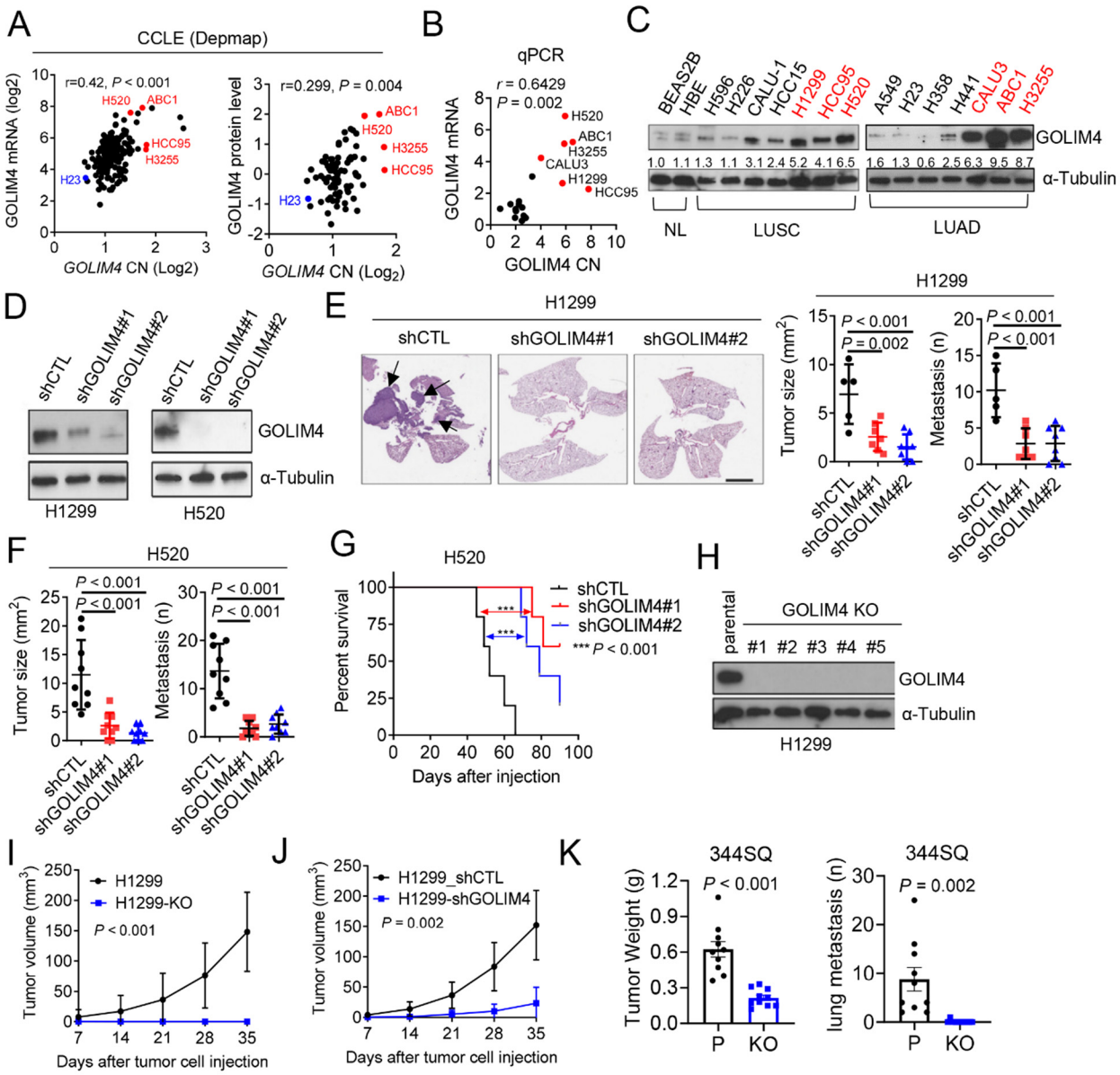

Figure 2. GOLIM4 is a pro-tumorigenic effector of the 3q amplicon. (A, B) Correlation analyses on 3q-amplified (red) and -diploid (black) lung cancer cell lines. (A) *GOLIM4* copy numbers, mRNA levels (left plot), and protein levels (right plot) in CCLE database. (B) Quantitative real-time PCR (qPCR) analysis of *GOLIM4* copy numbers and mRNA levels. (C) WB analysis of GOLIM4 levels. Immortalized lung epithelial cells (NL). (D) WB confirmation of target gene depletion in shRNA-transfected H1299 cells. GOLIM4 (shGOLIM4) or control (shCTL) shRNAs. (E and F) Orthotopic lung tumor size (left plots) and distant metastasis numbers (right plots) generated by shRNA-transfected H1299 cells (E) or H520 cells (F). Images: Hematoxylin and eosin (H&E)-stained lung

sections. (G) Kaplan-Meier survival analysis of orthotopic H520 orthotopic tumor-bearing mice. (H) WB confirmation of target gene depletion by Crispr/Cas-9-mediated gene editing in H1299 cells. Knockout (KO). (I) Sizes of flank tumors generated by cells in (H). Parental (H1299). (J) Sizes of flank tumors generated by cells in (D). (K) Primary tumor size (left plots) and lung metastasis numbers (right plots) generated by subcutaneously injected parental and *GOLIM4* KO 344SQ cells. Data indicate the mean ± SD from a single experiment incorporating biological replicate samples (n = 3, unless otherwise indicated) and are representative of at least 2 independent experiments. P values were determined using two-tailed student's t-test (for I-K), One-way ANOVA test (for E and F), or logrank test (for G).

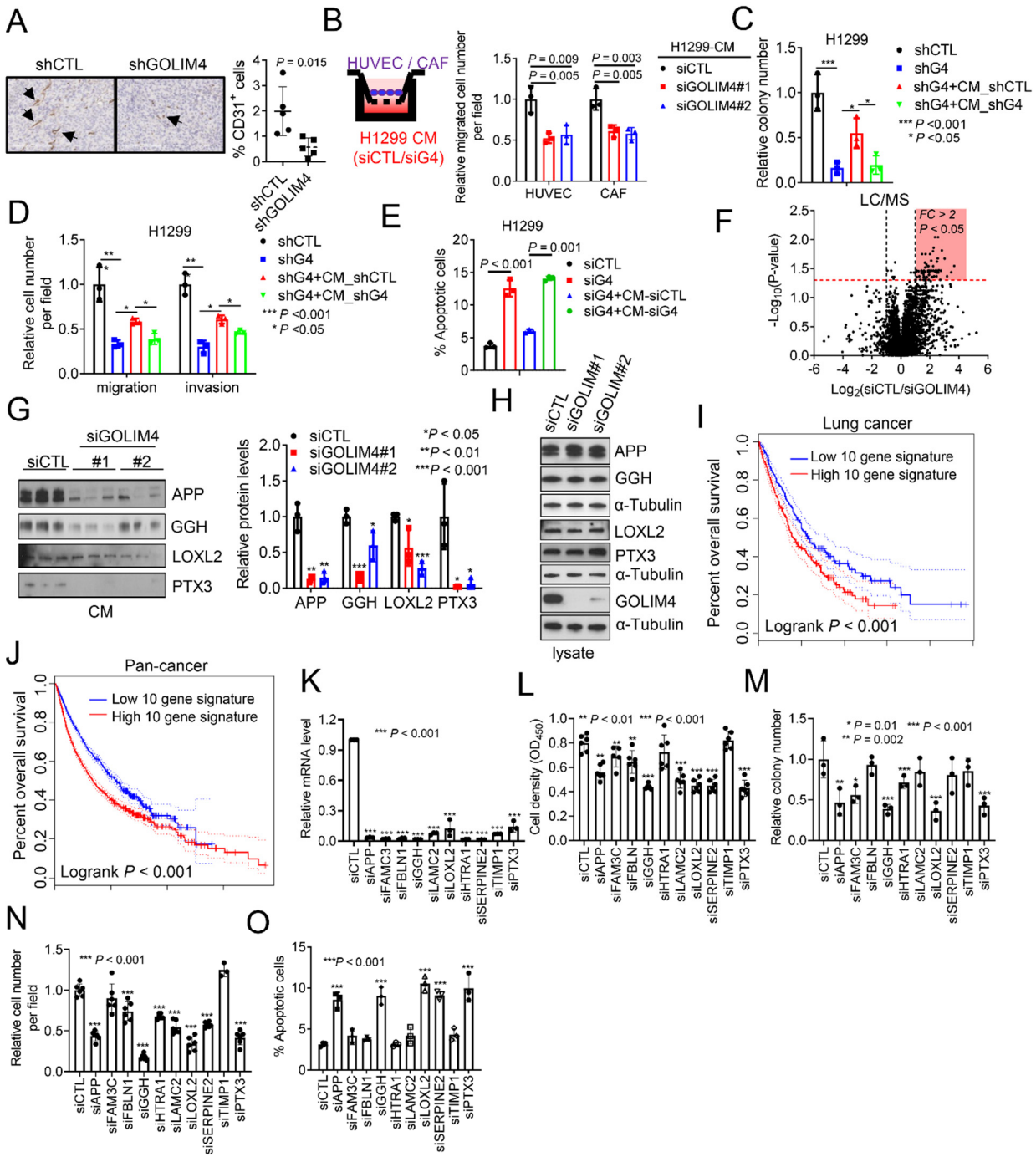

Figure 3. GOLIM4 activates a pro-tumorigenic secretory program. (A) Anti-CD31 antibody staining of tumors from (2J). Results expressed as percentages of total cells analyzed. (B) Boyden chamber assays to quantify recruitment of human umbilical vein endothelial cells (HUVEC) or cancer associated fibroblasts (CAF) by conditioned medium (CM) samples from siRNA-transfected H1299 cells. (C and D) Soft agar colony formation (C) and Boyden chamber migration and invasion (D) assays on shRNA-transfected H1299 cells treated with CM samples from shRNA-transfected H1299 cells. shGOLIM4 (shG4). Values expressed relative to shCTL. (E) Annexin V/propidium iodide flow cytometry on siRNA-transfected H1299 cells to detect apoptosis

following treatment with CM samples. (F) Volcano plot of proteins identified by LC-MS analysis of CM samples from siRNA-transfected H1299 cells. Results expressed as a log2 ratio (siCTL/siGOLIM4). Y-axis: p values; X-axis: fold-change. Proteins downregulated by siGOLIM4 (shaded areas). (G and H) WB analysis of proteins identified by LC-MS analysis. CM samples (G) and cell lysates (H) from siRNA-transfected H1299 cells. Densitometric analysis of bands in (G) expressed relative to siCTL (bar graph). (I and J) Kaplan-Meier survival analysis of the TCGA lung cancer (I) and pan-cancer (J) cohorts based on a ten-gene signature of GOLIM4-dependent secreted proteins. Tumors scored as above (high) or below (low) the median signature values for each cohort. $P < 0.001$. (K) qPCR confirmation of target gene depletion in siRNA-transfected H1299 cells. (L-O) Assessment of cells in (K) for relative densities in monolayer culture (L), colony formation in soft agar (M), invasion in Boyden chambers (N), and apoptosis by Annexin V/PI flow cytometry (O). Data indicate the mean ± SD from a single experiment incorporating biological replicate samples ($n = 3$, unless otherwise indicated) and are representative of at least 2 independent experiments. P values were determined using two-tailed student's t-test (for A), One-way ANOVA test (for B-E, G, and K-O) or logrank test (for I and J).

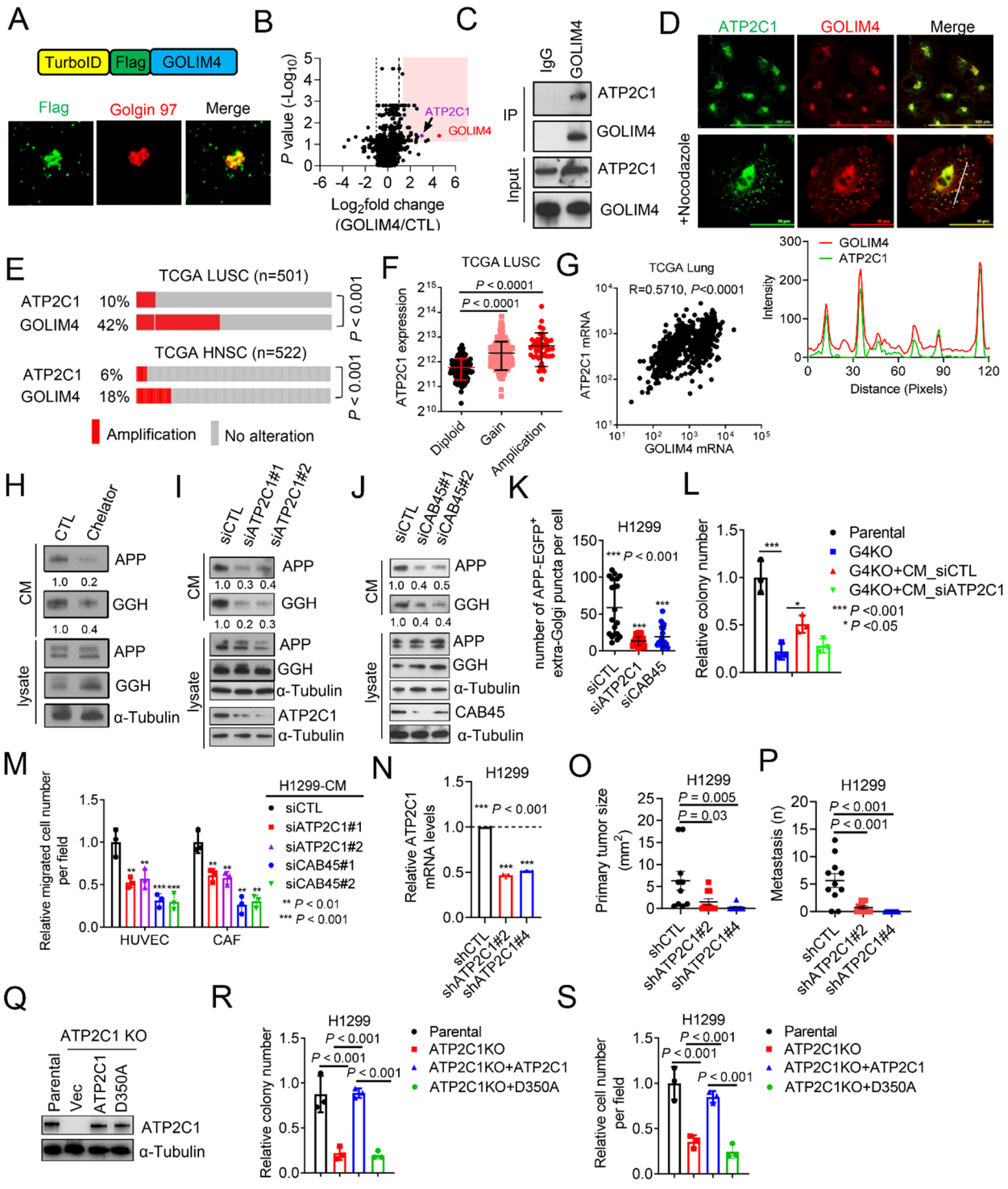

Figure 4. Functional cooperativity between 3q-amplified genes. (A) TurboID-GOLIM4 fusion construct (schema, top) localizes in the Golgi (confocal micrographs, bottom). H1299 cells transfected with TurboID-GOLIM4 and co-stained with anti-Flag, anti-GM130, and DAPI (blue). Single-channel and merged images. Scale bar: 50 μm. (B) Volcano plot of GOLIM4-associated proteins identified by TurboID-based proximity ligations assays. Results for each protein identified (dot) expressed as a log2 ratio (GOLIM4/CTL, X axis) and P value (Y axis). (C)

Immunoprecipitation (IP)/WB confirmation of ATP2C1 as a GOLIM4-associated protein in H1299 cells. (D) Confocal micrographs of endogenous ATP2C1 and GOLIM4 in H1299 cells. Cells treated with nocodazole to disperse the Golgi. Line plot (under images) assesses co-localization of GOLIM4 and ATP2C1. Signal intensities (y axis) and distances from plasma membrane (x axis). (E) Gene copy numbers (rows) in tumors (columns). Head and neck squamous cell carcinoma (HNSC). P <0.001, significant co-occurrence by one-sided Fisher's exact test. (F) Correlations between *ATP2C1* mRNA levels and gene copy numbers in tumors (dots). Diploid (n=109), gain (n=311), and amplification (n=48). (G) Pearson correlation between *GOLIM4* and ATPC1 mRNA levels in tumors (dots). (H-J) WB analysis of secreted protein levels in CM samples and cell lysates. H1299 cells treated with Ca chelator (H) or transfected with siRNAs against ATP2C1 (I) or Cab45 (J). (K) Number of APP-positive vesicles in H1299 cells transfected with indicated siRNAs. (L) Relative soft agar colony numbers generated by parental and *GOLIM4* KO (G4KO) H1299 cells following treatment with CM samples from siRNA-transfected H1299 cells. (M) Boyden chamber assays to quantify HUVEC and CAF recruitment by CM samples from siRNA-transfected H1299 cells. (N) qPCR confirmation of target gene depletion by ATP2C1 shRNAs in H1299 cells. (O and P) Orthotopic tumor size (O) and distant metastases (P) per mouse (dot) generated by H1299 transfectants in (N). (Q) WB confirmation of ATP2C1 reconstitution in *ATP2C1* KO cells by wild type or D350A-mutant ATP2C1. (R and S) Soft agar colony formation assay (R) and Boyden chamber migration assay (S) on cells generated in (Q). Data indicate the mean ± SD from a single experiment incorporating biological replicate samples (n = 3, unless otherwise indicated) and are representative of at least 2 independent experiments. P values were determined using One-way ANOVA test (for F, K-P, R, and S).

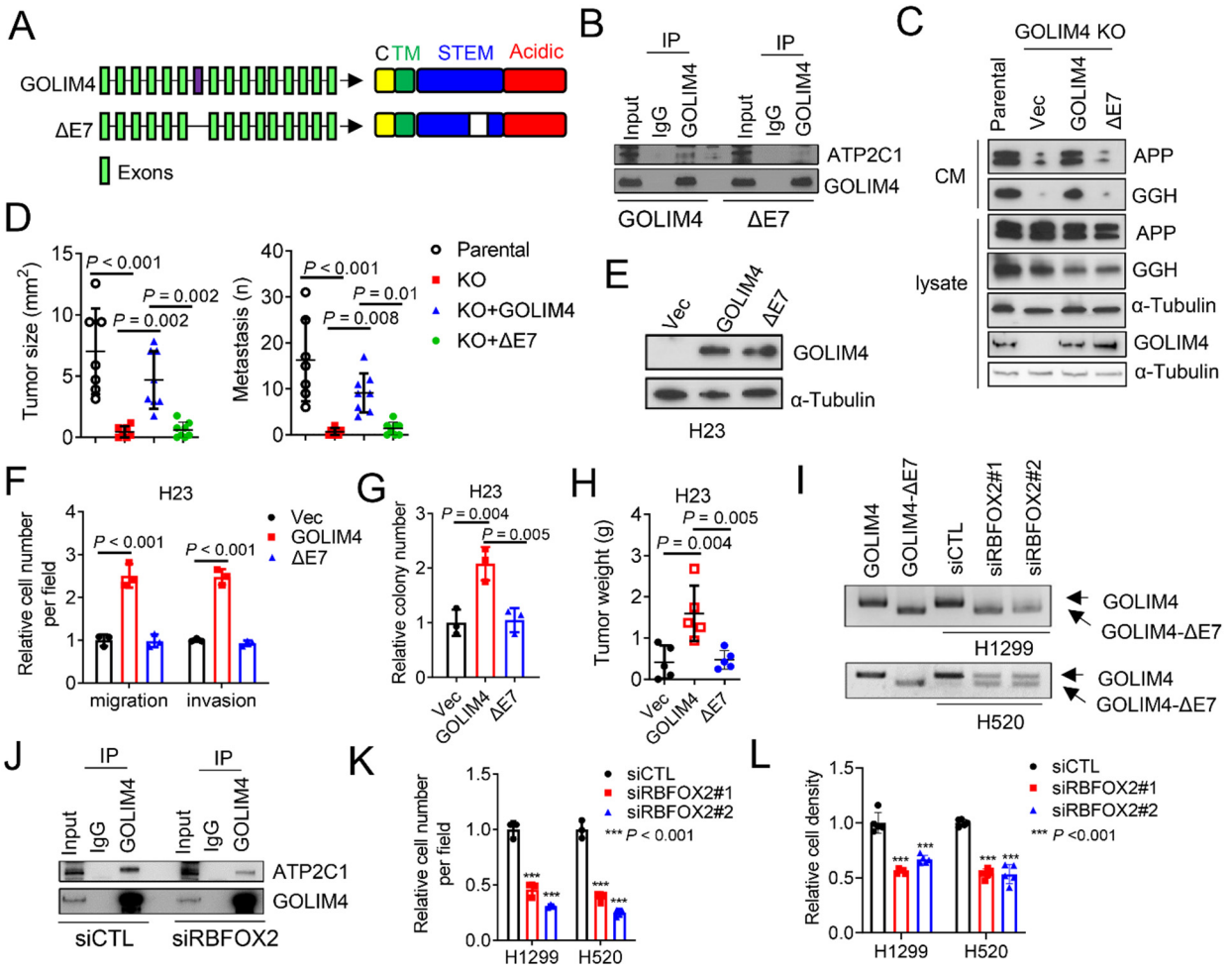

Figure 5. An alternatively spliced exon in *GOLIM4* is required for ATP2C1-binding and secretory activities. (A) Full-length and spliced (ΔE7) *GOLIM4* isoforms. Exon 7 located in intra-lumenal STEM domain. Transmembrane (TM), cytoplasmic (C) domains. (B) IP/WB analysis of GOLIM4 KO H1299 cells reconstituted with full length or ΔE7 GOLIM4. ATP2C1-binding activity detected only in full-length GOLIM4-transfected cells. (C) WB analysis of secreted proteins in CM samples and cell lysates from parental and *GOLIM4* KO H1299 cells reconstituted with full length or ΔE7 GOLIM4. Tubulin as loading control. (D) Quantification of orthotopic tumor size (left) and distant metastases (right) per mouse (dot) generated by H1299 cells in (C). (E) WB analysis of GOLIM4 levels in H23 cells transfected with full-length or ΔE7. Control vector (Vec). (F-H) Boyden chamber migration and invasion assays (F), soft agar colony assays (G), and flank tumor growth assays (H) on cells in (E). (I) RT-PCR analysis of *GOLIM4* isoforms in siRNA-transfected H1299 and H520 cells. Full-length and ΔE7 included as controls. (J) IP/WB analysis of H1299 cells demonstrates that FOXF2 depletion attenuates ATP2C1-binding activity of GOLIM4. (K and L) Boyden chamber migration assays (K) and relative cell density assays (L) on siRNA-transfected H1299 and H520 cells. Data indicate the mean ± SD from a single experiment incorporating biological replicate samples (n = 3, unless otherwise indicated) and are representative of at least 2 independent experiments. P values were determined using the one-way ANOVA test (for D, F-H, K, and L).

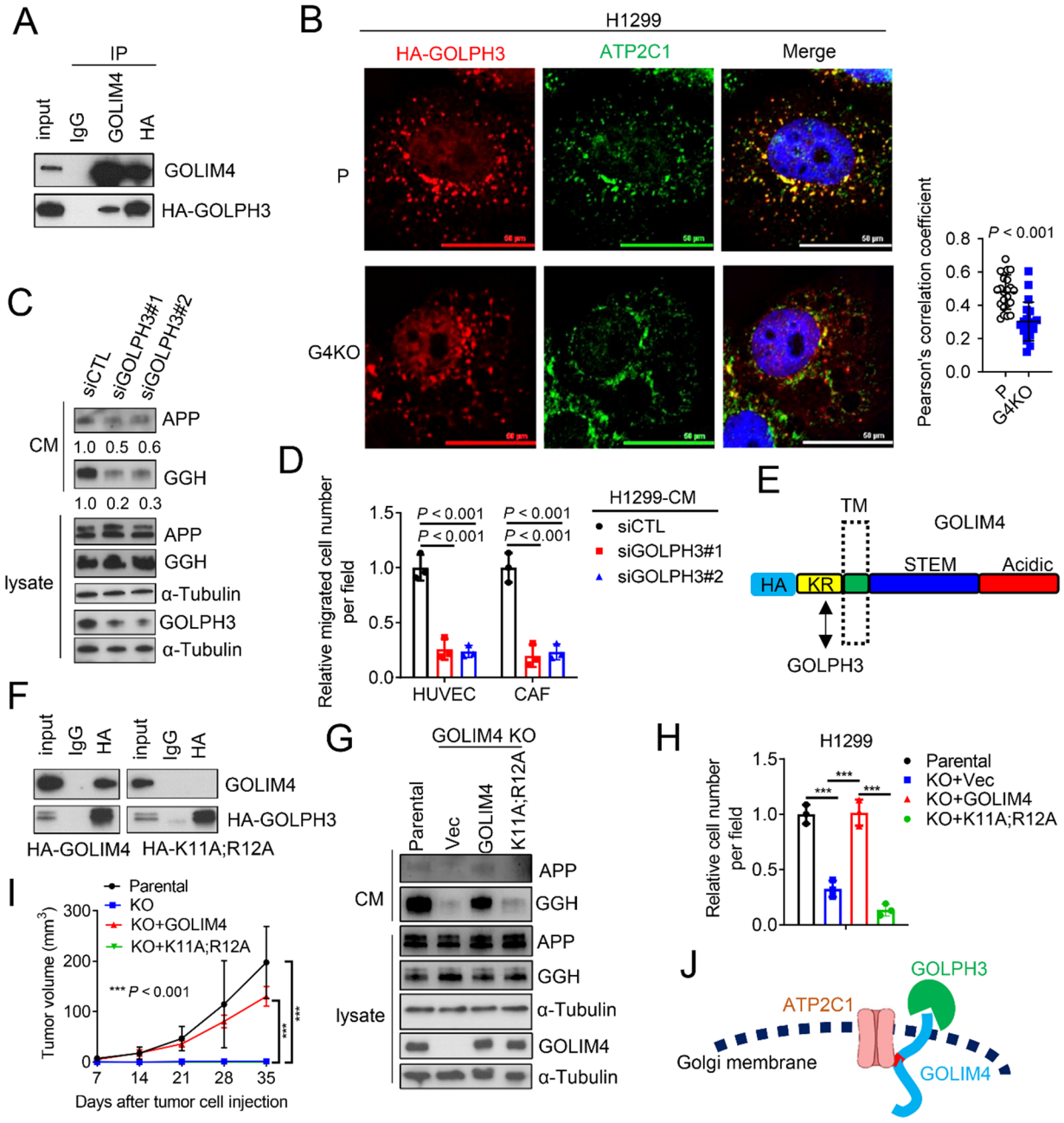

Figure 6. GOLPH3 is a GOLIM4 client protein that promotes secretion. (A) IP/WB analysis of H1299 cells detects HA-GOLPH3 in a GOLIM4-containing protein complex. (B) Confocal micrographs of H1299 cells transfected with HA-GOLPH3. Cells were treated with nocodazole to disperse the Golgi and co-stained with anti-HA and anti-ATP2C1. Scatter plot shows the percentages of HA-GOLPH3 that co-localize with ATP2C1 in each cell (dot). (C) WB analysis of secreted protein levels in CM samples and cell lysates following siRNA-mediated GOLPH3 depletion. Relative densitometric values under the gel lanes. α-Tubulin loading control. (D) Boyden chamber assays to quantify HUVEC and CAF recruitment by CM samples from siRNA-transfected H1299 cells. (E) GOLIM4 domain structure. KR residues required to bind to GOLPH3. HA tag, Transmembrane (TM), lumenal stem (STEM), and acidic domains. (F) IP/WB analysis of *GOLIM4* KO H1299 cells reconstituted with HA-tagged wild type (GOLIM4) or mutant

(K11A;R12A) GOLIM4. (G) WB analysis of secreted proteins in CM samples and lysates from *GOLIM4* KO H1299 cells reconstituted with wild-type or mutant GOLIM4. Empty vector (Vec). (H and I) Boyden chamber migration assays (H) and flank tumor growth assays (I) on cells generated in (G). (J) ATP2C1 and GOLPH3 are clients of the GOLIM4 scaffold. Data indicate the mean ± SD from a single experiment incorporating biological replicate samples (n = 3, unless otherwise indicated) and are representative of at least 2 independent experiments. P values were determined using two-tailed student's t test (for B) or one-way ANOVA test (for D, H, and I).

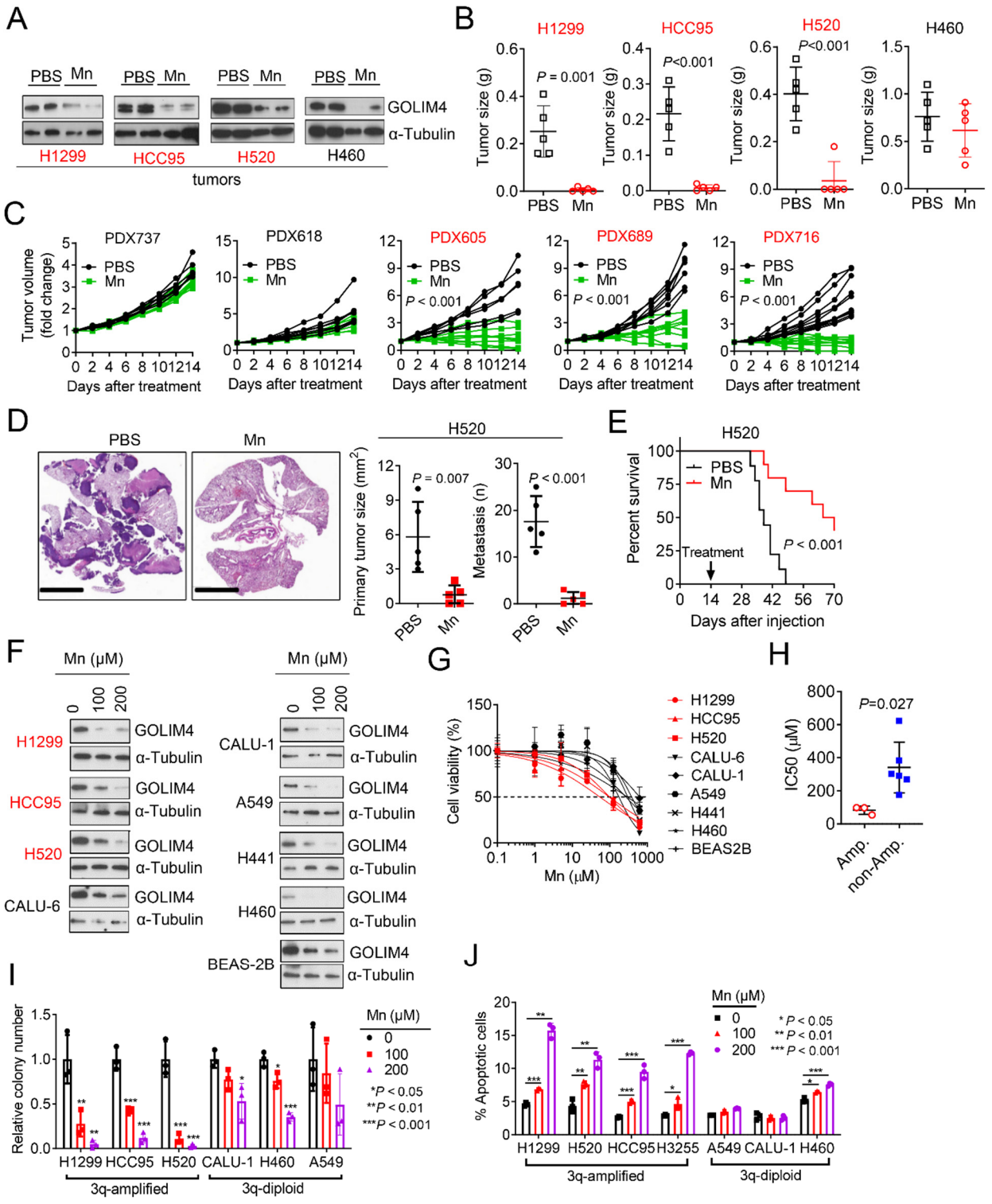

Figure 7. Mn treatment downregulates GOLIM4 levels and exerts selective anti-tumor activity in 3q-amplified lung cancer. (A-C) WB analysis of intra-tumoral GOLIM4 levels (A) and flank tumor weights generated by 3q-amplified (red) or -diploid (black) lung cancer cell lines (B) or LUSC patient-derived xenograft (PDX) models (C). Prior to sacrifice, mice were treated for 2 weeks with Mn or PBS. (D) Orthotopic tumor size (left plot) and metastasis numbers (right plot) generated by

H520 cells. H&E staining of lung sections. (E) Kaplan-Meier survival analysis of orthotopic H520 orthotopic tumor-bearing mice treated with Mn or PBS. (F) WB analysis of GOLIM4 levels in lung cancer cell lines treated with Mn. Immortalized human bronchial epithelial cells (BEAS-2B) included as control. (G) Relative densities of lung cancer cell lines treated for 4 d with different doses of Mn. (H) Half-maximal inhibitory concentrations (IC_{50}) from (G). (I and J) Soft agar colony formation assays (I) and Annexin V/PI flow cytometry-based apoptosis assays (J) on lung cancer cells treated with Mn. Data indicate the mean ± SD from a single experiment incorporating biological replicate samples (n = 3, unless otherwise indicated) and are representative of at least 2 independent experiments. P values were determined using two-tailed student's t test (for B-D, and H), one-way ANOVA test (for I and J), or logrank test (for E).

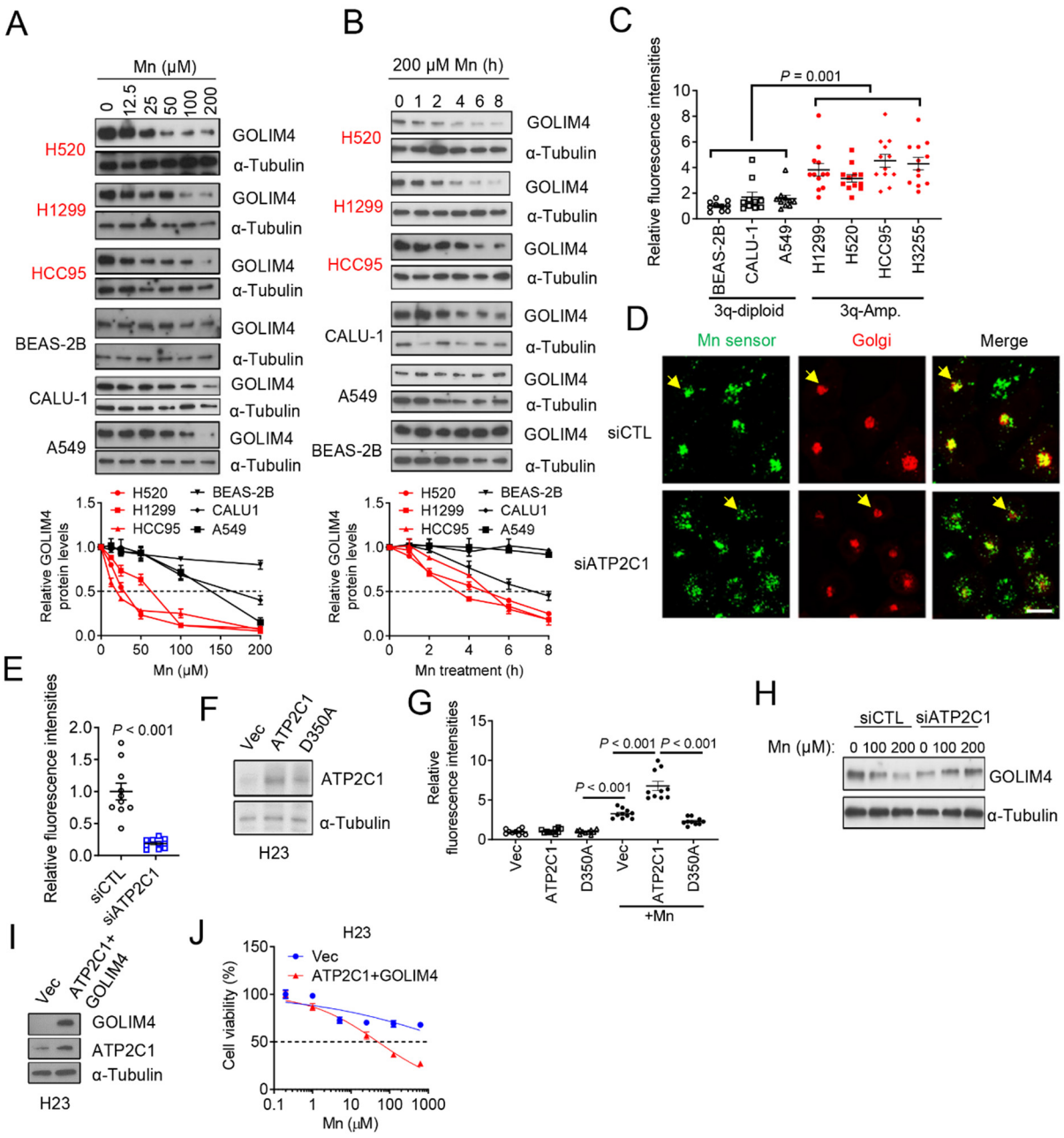

Figure 8. ATP2C1 sensitizes 3q-amplified lung cancer cells to Mn. (A and B) WB analysis of GOLIM4 levels in lung cancer cells treated with Mn in a dose-dependent (A) or time-dependent (B) manner. Densitometric quantification of GOLIM4 (line graphs). Values normalized to PBS-treated cells. (C) Intra-Golgi Mn sensor M1 activity in lung cancer cells (dots) treated with Mn. (D) Single-channel and merged confocal micrographs of Mn sensor M1 (green) in siRNA-transfected H1299 cells treated with Mn. CellLight Golgi-RFP (red). Scale bar: 100 μm. (E) Relative Mn sensor M1 intensity per cell (dot) in (D). (F) WB analysis of H23 cells stably transfected with wild-type (ATP2C1) or D350A-mutant ATP2C1. (G) Relative Mn sensor M1 intensity per cell (dot) after Mn treatment of cells generated in (F). (H) WB analysis of GOLIM4 levels in siRNA-transfected H1299 cells after Mn treatment. (I) WB analysis of H23 cells co-transfected with GOLIM4 and ATP2C1. Empty vector (Vec). (J) Relative densities of H23 cells in (I) treated with Mn. P < 0.001. Data

indicate the mean ± SD from a single experiment incorporating biological replicate samples (n = 3, unless otherwise indicated) and are representative of at least 2 independent experiments. P values were determined using two-tailed student's t test (for C, E, and J) or one-way ANOVA test (for G).